

Evidence for strong electron-phonon coupling in MgCNi₃

A. Wälte, G. Fuchs,* K.-H. Müller, A. Handstein, K. Nenkov,†
 V.N. Narozhnyi,‡ S.-L. Drechsler, S. Shulga,§ and L. Schultz

Institut für Festkörper- und Werkstoffforschung Dresden, Postfach 270116, D-01171 Dresden, Germany

H. Rosner

*Max-Planck-Institut für Chemische Physik fester Stoffe,
 Nöthnitzer Strasse 40, D-01187 Dresden, Germany*

(Dated: 1 August 2002)

The title compound is investigated by specific heat measurements in the normal and superconducting state supplemented by upper critical field transport, susceptibility and magnetization measurements. From a detailed analysis including also full potential electronic structure calculations for the Fermi surface sheets, Fermi velocities and partial densities of states the presence of both strong electron-phonon interactions and considerable pair-breaking has been revealed. The specific heat and the upper critical field data can be described to first approximation by an effective single band model close to the clean limit derived from a strongly coupled predominant hole subsystem with small Fermi velocities. However, in order to account also for Hall-conductivity and thermopower data in the literature, an effective general two-band model is proposed. This two-band model provides a flexible enough frame to describe consistently all available data within a scenario of phonon mediated *s*-wave superconductivity somewhat suppressed by sizeable electron-paramagnon or electron-electron Coulomb interaction. For quantitative details the relevance of soft phonons and of a van Hove type singularity in the electronic density of states near the Fermi energy is suggested.

PACS numbers: 74.70.Ad, 74.60.Ec, 74.60.Ge

Keywords: A. Superconductors, D. Upper critical field, Specific heat

I. INTRODUCTION

The recent discovery of superconductivity in the intermetallic antiperovskite compound MgCNi₃¹ with a superconducting transition temperature of $T_c \simeq 8$ K is rather surprising considering its high Ni content. Therefore it is expected that this compound is near a ferromagnetic instability which might be reached by hole doping on the Mg sites.² The possibility of unconventional superconductivity due to the proximity of these two types of collective order has attracted great interest in the electronic structure and the physics of the pairing mechanism.

Band structure calculations^{2,3,4,5,6} for MgCNi₃ revealed a domination of the electronic states at the Fermi surface by the *3d* orbitals of Ni, suggesting presence of ferromagnetic spin fluctuations.^{2,4} ¹³C NMR measurements⁷ result in Fermi liquid behavior with an electronic crossover at $T \approx 50$ K, growing formation of spin fluctuations below $T \approx 20$ K. Resistivity measurements,^{1,8,9} measurements of the thermopower, the thermal conductivity and the magnetoresistance,¹⁰ doping experiments^{9,11} and magnetization measurements¹¹ are consistent with this interpretation.

MgCNi₃ can be considered as the 3-dimensional analogue of the quaternary layered transition metal borocarbides which exhibit superconducting transition temperatures up to $T_c \simeq 23$ K. In spite of the much lower T_c of MgCNi₃, its upper critical field H_{c2} at low temperatures, $H_{c2}(0) = 8 \dots 15$ T,^{8,12,13,14,15} is comparable with that

of the borocarbides or even higher. However, a rather different shape, especially near T_c , for the temperature dependence of $H_{c2}(T)$ is observed for these compounds. The $H_{c2}(T)$ dependence of MgCNi₃ is similar to that of usual (standard) intermetallic superconductors which are described reasonably well within the isotropic single-band approximation and exhibit a steep slope of $H_{c2}(T)$ at T_c .

Through analysis of specific heat data, MgCNi₃ was characterized in the framework of a conventional, phonon-mediated pairing both as a moderate^{1,15} and as a strong^{13,16} coupling superconductor. Strong coupling is also suggested by measurements of the thermopower¹⁰ and the large energy gap determined from tunneling experiments.¹³ The question of the pairing symmetry is controversially discussed in the literature. ¹³C NMR experiments,⁷ specific heat measurements¹⁵ and tunneling spectra¹⁷ support *s*-wave pairing in MgCNi₃, whereas earlier tunneling spectra¹³ and penetration depth measurements¹⁸ have been interpreted in terms of an unconventional pairing state. Recent measurements of the critical current of MgCNi₃ may be interpreted in the latter sense, too.¹⁹

In the present investigation, specific heat data of MgCNi₃ in the normal and superconducting state were analyzed in detail with the aid of a realistic phonon model and strong coupling corrections as suggested by Carbotte.²⁰ The results are brought into accordance with the two-band character of MgCNi₃ emerging from band structure calculations and a parallel analysis of the upper critical field $H_{c2}(0)$, in order to find out a consistent physical picture explaining at least qualitatively various

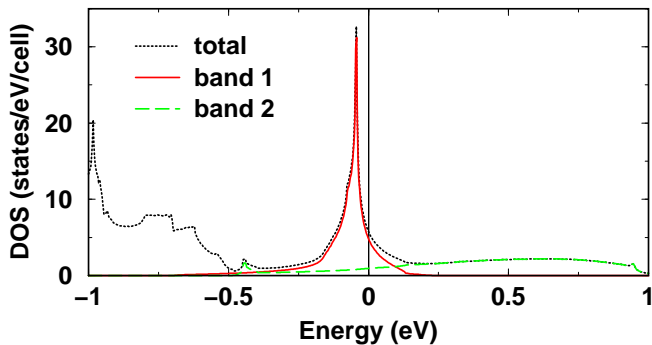


FIG. 1: Partial density of states of the two bands in MgCNi_3 corresponding to the two Fermi surface sheets shown in Fig. 2. Dotted line: total density of states.

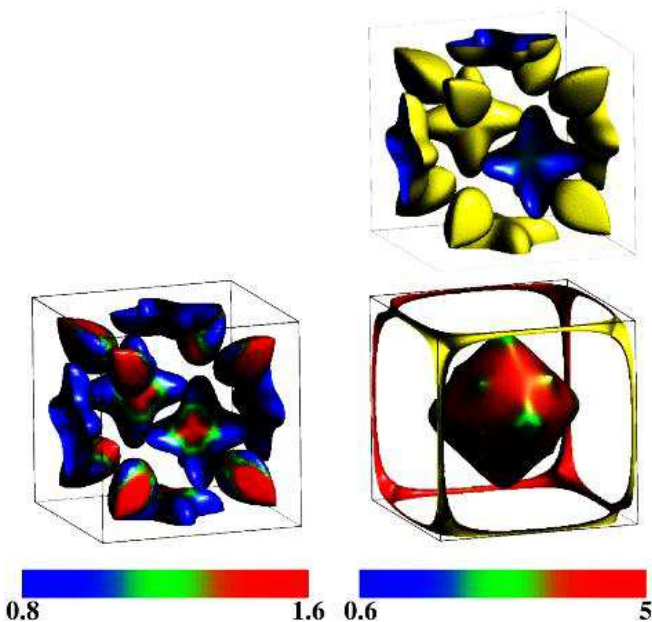


FIG. 2: Fermi surface sheets of MgCNi_3 . Fermi velocities are measured in different colors (see scales below the figure) in units of 10^7 cm/s, i.e. blue color stands for slow and red color for fast quasiparticles. Upper panel and lower left panel: hole sheets corresponding to “band 1” in Fig. 1. Lower right panel: electron sheets corresponding to “band 2” in Fig. 1. The right panels present the Fermi velocity distribution of the two sheets on the same absolute scale to demonstrate the slow (heavy) character of the holes. Yellow color: sides of filled electrons. The left panel shows the v_F -distribution in the hole sheets on a smaller scale in more detail.

available experimental results.

II. ESSENTIALS OF THE THEORETICAL ELECTRONIC STRUCTURE

Following previous work of one of the authors (H.R.)² in the present section we remind the reader on some essential features and point out important, but neverthe-

less so far unpublished details of the electronic structure of MgCNi_3 which are crucial for a proper interpretation of the specific heat (total and Fermi surface sheet (FSS) related partial densities of states (DOS)), upper critical field and transport data (topology of the Fermi surface and the magnitude of the Fermi velocities). Among various band structure calculations there is general consensus about the qualitative topology of the Fermi surface and the presence of a strong peak (Van Hove Singularity) in $N(E)$ slightly below the Fermi energy. At the same time there are clear differences with respect to the magnitudes of $N(0) = 4.8$ states/eV = 11 mJ/molK² (to be compared with 4.63 states/eV,³ 4.99 states/eV,⁴ 5.34 states/eV⁶) and especially with respect to the Stoner factor $S = 3.3$ (compared with 1.75,³ 2.78,²¹ to 5,⁴) as well as to the distance of the DOS peak 42 meV (compared with 40 meV²² to 80 meV²¹) below E_F . The peak may be of relevance for a proper quantitative description of the electronic specific heat, transport data, magnetic properties, and the superconductivity. Last but not least, there is also a sizeable disparity on the magnitude of the electron-phonon coupling constant λ_{ph} (ranging between 0.8...2.0) mainly caused by the poor knowledge of the phonon energies and possible lattice anharmonicities.²²

Our results have been obtained by a band structure calculation code using the full-potential nonorthogonal local-orbital (FPLO) minimum-basis scheme.²³ There are about 0.285 charges per unit cell with exactly equal numbers of holes and electrons, i.e. $n_h = n_{el}$ which follows from the even number of electrons per unit cell. In other words, MgCNi_3 is a so called compensated metal which must be described in terms of multi-band model by definition (per sé). Thus, it makes sense to start with a two-band model. The generalization to any higher multi-band scenario is straightforward. A standard single band system with an even number of electrons per unit cell would be an insulator and not a superconductor. Thus metallicity is achieved owing to the two-band character which leads to electron and hole derived Fermi surface sheets (FSS). The total DOS $N(0)$ at the Fermi level can be decomposed into a roughly 85% and a 15% contribution stemming from two hole and two electron sheets of the Fermi surface, respectively (see Figs. 1, 2). On the Fermi surface sheets shown in Fig. 2 the sides of filled electron states are shown in yellow/gold color. The two types of hole sheets are formed by eight droplets (ovoids) oriented along the spatial diagonals of the cube, i.e. along the Γ -R lines and six FSS with a “four-leaved clover”-like shape centered at the X-points in the middle of the faces of the cube (see Fig. 2). The coordinates of the symmetry points read $\Gamma = (0, 0, 0)$, $R = (0.5, 0.5, 0.5)$, $X = (0.5, 0, 0)$ and $M = (0.5, 0.5, 0)$ (all given in units of $2\pi/a$, where $a = 0.381$ nm is the lattice constant). The FSS with electron character are given by the rounded cube centered at Γ and 12 thin jungle gims spanning from R to M.

The band structure calculations provide us directly with several material parameters (total and partial den-

sities of states, Fermi velocities, etc.) important for the understanding of superconductivity and electronic transport properties. For instance the transport properties are described by quadratically averaged Fermi velocities: $\langle v^2 \rangle_{\text{FSS}}$ whereas the upper critical field is described by averages of the type $\langle 1/v^2 \rangle_{\text{FSS}}$ which yields a smaller effective velocity in general. Using the general definitions of the local density of states (in \vec{k} -space) and those of m^{th} and the first moments of the Fermi velocity $v = \left| \vec{v} \left(\vec{k} \right) \right|$, respectively, we have

$$\begin{aligned} \langle v^m \rangle_i &= \frac{\int dS_i N_i \left(\vec{k} \right) \left| v_i \left(\vec{k} \right) \right|^{m-1}}{\int dS_i N_i \left(\vec{k} \right)} \\ &\equiv \frac{\int dS_i \left| \vec{v}_i \left(\vec{k} \right) \right|^{m-1}}{4\pi^3 \hbar N_i(0)}, \\ \langle v \rangle_i &\equiv \bar{v}_i \\ &= \frac{S_{F,i}}{4\pi^3 \hbar N_i(0)}, \\ \langle v^m \rangle_i &= \frac{\bar{v}_i \int dS_i \left| \vec{v} \left(\vec{k} \right) \right|^{m-1}}{S_{F,i}}, \end{aligned}$$

where $i = el, h, tot$ and $S_{f,i}$ denotes the area of the i^{th} Fermi surface sheet and the effective quantity is related to the linearly averaged value \bar{v} adopting a simple estimate as

$$\begin{aligned} \langle v^{-2} \rangle_i &= \frac{\bar{v}_i \int dS_i \left| \vec{v}_i \left(\vec{k} \right) \right|^{-3}}{S_{F,i}} \equiv v_{hc2,i}^{-2}, \\ v_{hc2} &\approx \bar{v} \left[1 - (\delta v / \bar{v})^2 \right], \end{aligned}$$

where δv is the halfwidth of the v_F distribution. For the two above mentioned subgroups of quasiparticles we estimate: $\bar{v}_2 = 3.9 \times 10^7$ cm/s and $\bar{v}_1 = 1.2 \times 10^7$ cm/s, $v_{tr,1} = 1.11 \times 10^7$ cm/s, $v_{hc2,1} = 1.07 \times 10^7$ cm/s and $v_{tr,2} = 4.89 \times 10^7$ cm/s, where $\delta v_1 = 4 \times 10^6$ cm/s and $\delta v_2 = 1.1 \times 10^7$ cm/s have been used (compare also Fig. 2).

Finally, in the isotropic single band (ISB) model realized in the extreme dirty limit of superconductivity one arrives at

$$N(0)v_{tr,ISB}^2 = N_1(0)v_{tr,1}^2 + N_2(0)v_{tr,2}^2,$$

which yields $v_{tr,ISB} = 2.15 \times 10^7$ cm/s in accordance with Ref. 3. The corresponding plasma energy amounts $\hbar\omega_{pl} = 3.17$ eV close to 3.25 eV given in Ref. 4. Naturally, the total plasma frequency ω_{pl} can be also decomposed into the plasma frequencies of both subsystems

$$\omega_{pl}^2 = \omega_{pl,1}^2 + \omega_{pl,2}^2 = \omega_{pl,1}^2 \left(1 + \frac{N_2(0)v_{tr,2}^2}{N_1(0)v_{tr,1}^2} \right).$$

Thus we estimate $\hbar\omega_{pl,1} \equiv \hbar\omega_{pl,h} \approx 1.89 \dots 1.94$ eV and $\hbar\omega_{pl,2} \equiv \hbar\omega_{pl,el} \approx 2.55 \dots 2.61$ eV. From these partial plasma energies a useful relation between the scattering rates γ_i and the conductivities σ_i (with $i = 1, 2$) in both subsystems can be obtained:

$$\frac{\gamma_{el}}{\gamma_h} = 1.816 \frac{\sigma_h}{\sigma_{el}} = 1.816 \frac{\rho_{el}}{\rho_h},$$

where ρ_i denotes the corresponding resistivity. In the present case the disorder is expected to be caused mainly by Mg and C related defects such as vacancies and interstitials. Therefore the ratio of the scattering rates might scale with the ratio of the non-Ni derived Mg and C orbital partial densities of states at the Fermi level and the corresponding Fermi velocities. As a result we estimate from our LDA-FPLO calculations

$$\left(\frac{\gamma_{el}}{\gamma_h} \right)_{\text{LDA}} \approx \frac{N_{el,Mg,C}(0)v_{F,el}}{N_{h,Mg,C}(0)v_{F,h}} \approx 4.81. \quad (1)$$

Within this approach the corresponding mean free paths differ by a factor of 0.917 and a conductivity ratio of $\sigma_h/\sigma_{el} = 1.403$ would be expected.

In the following analysis we usually make use of $\hbar = k_B = \mu_0 = 1$ for the sake of simplification.

III. EXPERIMENTAL

Polycrystalline samples of MgCNi₃ have been prepared by solid state reaction. In order to obtain samples with high T_c , we used an excess of carbon as proposed in Ref. 1. To cover the high volatility of Mg during sintering of the samples an excess of Mg is used.¹ In this study, a sample with the nominal formula Mg_{1.2}C_{1.6}Ni₃ has been investigated and is denoted as MgC_{1.6}Ni₃. To prepare the sample a mixture of Mg, C and Ni powders was pressed into a pellet. The pellet was wrapped in a Ta foil and sealed in a quartz ampoule containing an Ar atmosphere at 180 mbar. The sample was sintered for half an hour at 600°C followed by one hour at 900°C. After a cooling process the sample was reground. This procedure was repeated two times in order to lower a possible impurity phase content. The obtained sample was investigated by x-ray diffractometry to estimate its quality. The diffractometer pattern (Fig. 3) shows small impurity concentrations mainly resulting from MgO and unreacted carbon crystallized as graphite (≈ 10 vol-%). The lattice constant of the prepared sample was determined to be $a = 0.38107(1)$ nm using the Rietveld code FULLPROF.²⁴ This indicates that the nearly single-phase sample corresponds to the superconducting modification of MgC_xNi₃.²⁵ The superconducting transition of the sample was investigated by measurements of electrical resistance, ac susceptibility and specific heat. For the electrical resistance measurement a piece cut from the initially prepared pellet with 5 mm in length and a

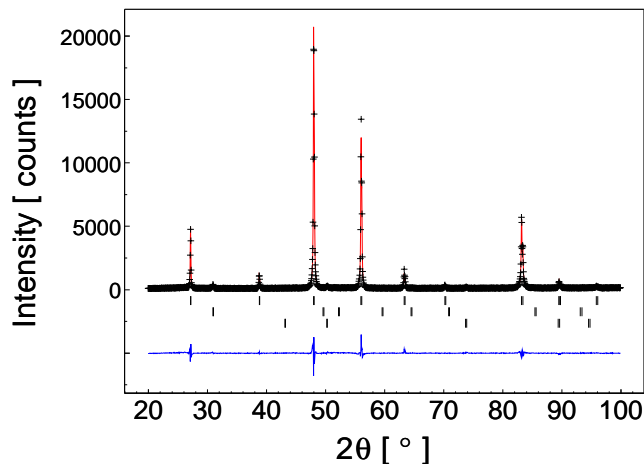


FIG. 3: Rietveld refinement for the $\text{MgC}_{1.6}\text{Ni}_3$ sample. The crosses correspond to the experimental data. The black line shows the calculated pattern. The vertical bars give the Bragg positions for the main phase MgCNi_3 , for graphite and MgO (from top to bottom). The black line at the bottom of the plot gives the difference between the experimental and calculated pattern.

cross section of approximately 1 mm^2 was measured in magnetic fields up to 16 T using the standard four probe method with current densities between 0.2 and 1 A/cm^2 . The ac susceptibility and the specific heat measurements were performed on other pieces from the same pellet in magnetic fields up to 9 T.

IV. RESULTS

A. Resistivity

The temperature dependence of the electrical resistance of the investigated sample is shown in Fig. 4. A superconducting transition with an onset (midpoint) value of $T_c = 7.0 \text{ K}$ (6.9 K) is observed (see inset of Fig. 4) which coincides with the onset of the superconducting transition of $T_c = 7.0 \text{ K}$ determined from ac susceptibility. Its residual resistance ratio $\rho(300\text{K})/\rho(8\text{K}) = 1.85$ and the shape of the $\rho(T)$ curve are typical for MgCNi_3 powder samples.^{1,8,9} It should be noted, that the sample of Fig. 4 has a resistivity of $\rho_{300\text{K}} = 2.1 \text{ m}\Omega\text{cm}$ which is much too large in order to be intrinsic.

A natural explanation for the high resistivity of the investigated sample which was not subjected to high pressure sintering is a relatively large resistance of the grain boundaries.⁹ In this context the recent low-resistivity thin film data (with ρ_0 down to $20 \mu\Omega\text{cm}$) by Young et al.¹⁴ are of interest, since in that case similar values of the upper critical field and T_c just as in the best powder samples⁸ have been observed.

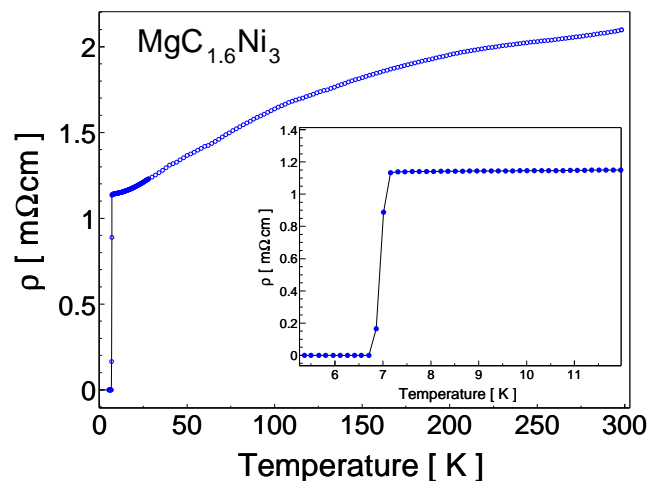


FIG. 4: Resistivity as a function of temperature of the $\text{MgC}_{1.6}\text{Ni}_3$ sample up to room temperature. The inset shows the superconducting transition region.

B. Specific heat

Specific heat measurements were performed in order to get information about the superconducting transition, the upper critical field and the superconducting pairing symmetry and the strength of the electron-phonon coupling from thermodynamic data. In Fig. 5 specific heat data, c_p/T vs. T^2 , are shown for applied magnetic fields up to 8 T. The previously mentioned (see Sec. III) 10 vol.-% graphite impurity contribution was subtracted according to Ref. 26.

The specific heat can be considered as a sum of a lattice contribution and a linear-in- T term which gives the electronic contribution with γ_N^* as the Sommerfeld parameter:

$$c_n(T) = \gamma_N^* T + c_{\text{lattice}}(T). \quad (2)$$

To extract the lattice contribution of the normal state specific heat the low temperature limit

$$c_{\text{lattice}}(T) = \beta T^3 \quad (3)$$

of the Debye model is usually applied. A fit of Eq. (2) to the data is shown in Fig. 5 resulting the parameters $\beta = 0.39 \text{ mJ}\text{K}^2/\text{mol}$ and $\gamma_N^* = 27.0 \text{ mJ}/\text{mol}\text{K}^2$. Notice, that the Sommerfeld parameter is connected to the electron-phonon coupling strength by $\gamma_N^* = \gamma_0(1 + \lambda_{\text{ph}})$. With $\gamma_0 = 11 \text{ mJ}/\text{mol}\text{K}^2$ (Sec. II), one obtains $\lambda_{\text{ph}} = 1.45$ in contradiction with recently reported medium coupling results.^{1,15} From the lattice contribution the Debye temperature $\Theta_D^* = 292 \text{ K}$ was derived. Both parameters (Θ_D^* , γ_N^*) are consistent with what has been reported so far.^{13,15} The fit describes the normal state data above T_c but its extrapolation to $T = 0 \text{ K}$ obviously underestimates the high-field data (see Fig. 5).

The transition temperature, $T_c = 6.8 \text{ K}$, calculated from entropy conservation criterion, agrees well with the

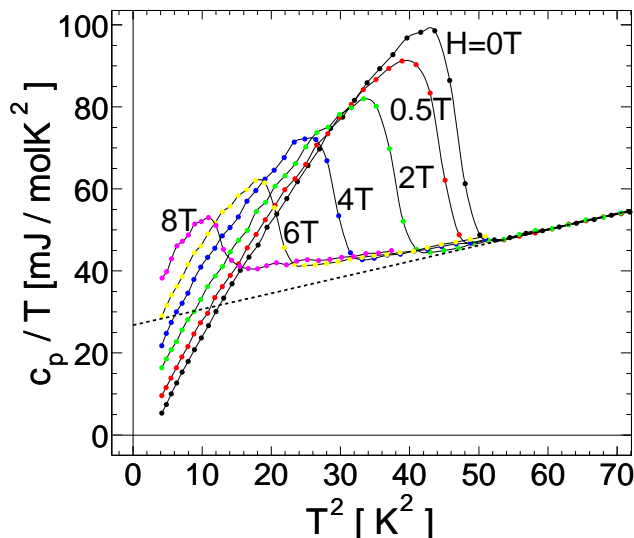


FIG. 5: Specific heat data c_p/T vs. T^2 of $\text{MgC}_{1.6}\text{Ni}_3$ measured at various magnetic fields up to 8 T. The dashed line is a fit of the Debye approximation to the data for $H = 0$ T above T_c . Its intersection with the c_p/T -axis gives the Sommerfeld parameter $\gamma_N^* = 27$ mJ/molK² (see text).

transition temperatures $T_c = 6.9$ K and $T_c = 7.0$ K derived from resistance and from ac susceptibility data, respectively.

The jump $\Delta c(T = T_c)$ of the specific heat is given by the difference between the experimental data, $c_p(T)$ and the normal state specific heat contribution $c_n(T)$. Notice that the experimental value of the jump, $\Delta c(T_c)/(\gamma_N T_c) = 2.09$ (derived from an entropy conserving construction – see Sec. V C) is strongly enhanced compared to the BCS value (1.43), indicating strong electron-phonon coupling.

C. Superconducting transition and upper critical field

The field dependence of the electrical resistance of our investigated sample is shown in Fig. 6 for several temperatures between 1.9...6.0 K. A sharp transition is observed. It remains sharp down to low temperatures. In Fig. 7, the field values H_{10} , H_{50} and H_{90} defined at 10 %, 50 % and 90 % of the normal state resistance are plotted as function of temperature. Identical results have been found from resistance-vs.-temperature transition curves measured at different magnetic fields. Additionally, Fig. 7 shows upper critical field data determined from ac susceptibility measurements, H_{c2}^{sus} , determined by an onset criterion.

It is clearly seen that for the investigated sample H_{c2}^{sus} agrees approximately with H_{10} . A similar behavior was already observed for MgB_2 , whereas in the case of rare-earth nickel borocarbides the onset of superconductivity

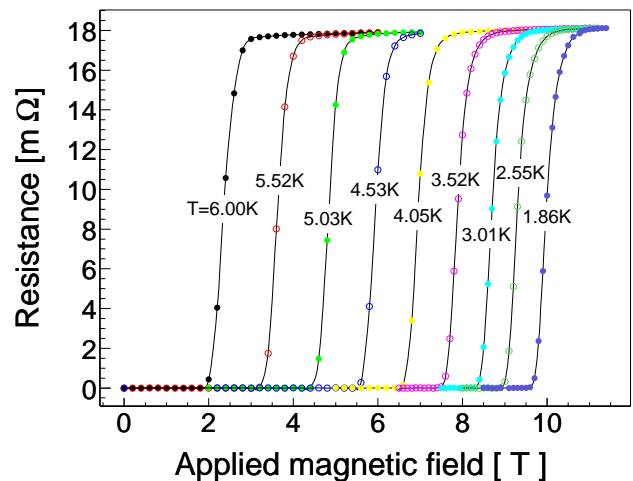


FIG. 6: Resistivity of the $\text{MgC}_{1.6}\text{Ni}_3$ sample as a function of the applied magnetic field for various fixed temperatures as labeled.

determined from ac susceptibility was typically found to agree well with the midpoint value (H_{50}) of the normal state resistivity. The width $\Delta H = H_{90} - H_{10}$ of the superconducting transition curves in Fig. 6 (and Fig. 7) remains, with $\Delta H \simeq 0.6$ T, almost unchanged down to low temperatures. A non-textured polycrystalline sample of a strongly anisotropic superconductor shows a gradual broadening of the superconducting transition with decreasing temperature as was observed, for example, for MgB_2 .²⁷ Therefore, the nearly constant transition width ΔH observed for the investigated sample can be considered as an indication of a rather small anisotropy of $H_{c2}(T)$ in MgCNi_3 .

The upper critical fields, $H_{c2}(T)$, determined from the specific heat data, are shown in Fig. 8. The $H_{c2}(T)$ data obtained from the specific heat are located in the small field range between the $H_{90}(T)$ and $H_{10}(T)$ curves determined from resistivity measurements (see Fig. 6).

The extrapolation of $H_{90}(T)$ to $T = 0$ K yields an upper critical field of $H_{c2}(0) \simeq 11.0$ T (see Fig. 7). The observed temperature dependence of the upper critical field is typical for $H_{c2}(T)$ data reported for MgCNi_3 so far¹⁶ and was described^{8,13,15} within the standard WHH model²⁸ by conventional superconductivity. However, a quantitative analysis of H_{c2} data presented in Sec. VI A shows that the magnitude of the upper critical field $H_{c2}(0)$ at $T = 0$ K can be understood only if strong electron-phonon coupling is taken into account.

V. ANALYSIS

A. Resistivity in the normal state

The non-intrinsic origin of the residual resistivity $\rho_{0\text{K}} \approx 1.13$ mΩcm follows from physically reasonable val-

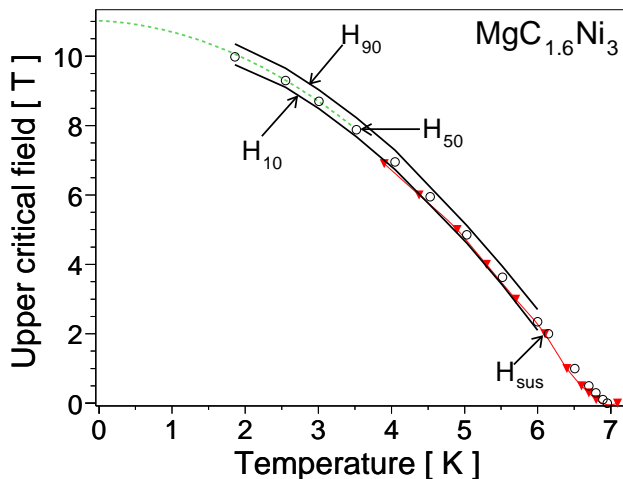


FIG. 7: The upper critical field as a function of temperature. The circles show the midpoint of the transition (H_{50}). The two lines labeled H_{10} and H_{90} denote 10 % and 90 % of normal state resistivity. The triangles represent the upper critical field from susceptibility measurements (onset values). The dashed line illustrates the extrapolation of the resistivity data to $T = 0$ K.

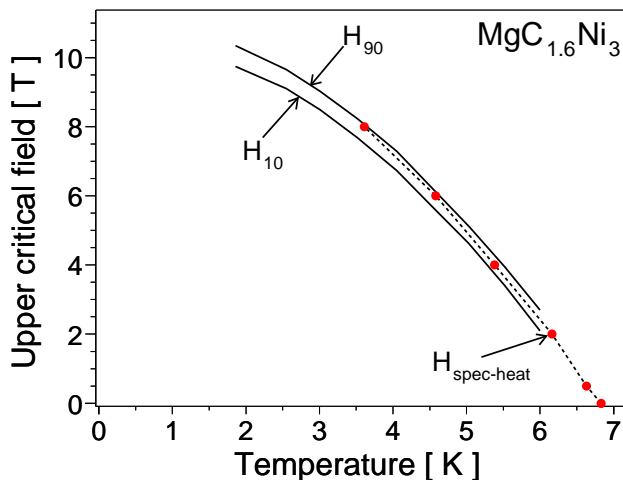


FIG. 8: Comparison of upper critical field data determined from specific heat (\bullet) and resistance measurements. H_{10} and H_{90} were determined at 10% and 90% of the normal state resistivity, respectively. An entropy conserving construction was used to determine the upper critical field from the specific heat data of Fig. 5.

ues for the mean free path l given by

$$l_{\text{imp}} = \frac{4\pi v_F}{\omega_{\text{pl}}^2 \rho_0}$$

or in more convenient practical units

$$l_{\text{imp}}[\text{nm}] = 4.9 \times 10^2 \frac{v_F [10^7 \text{ cm/s}]}{(\hbar\omega_{\text{pl}}[\text{eV}])^2 \rho_0 [\mu\Omega\text{cm}]}, \quad (4)$$

TABLE I: Debye and Einstein temperatures with corresponding occupation numbers. D_i denote the acoustic phonons and E_i the optical phonons. Θ gives the corresponding temperature and ν_i is the grouping parameter, giving the number of modes found to have the same temperature.

	acoustic modes			optical modes			
	D1	D2	E1	E2	E3	E4	E5
Θ [K]	129	316	86	163	256	472	661
ν_i	1	2	0.33	2.67	3	3	3

with ρ_0 as the residual resistivity. In the isotropic single band (ISB) case, with $v_F = v_{\text{tr,ISB}} \approx 2 \times 10^7$ cm/s and the plasma energy $\hbar\omega_{\text{pl}} \approx 3$ eV (see Sec. II), one arrives at the conclusion, that in fact, in the m Ω cm range, typical for most powder samples considered so far in the literature, even at $T = 0$ K the mean free path l – given by Eq. (4) – would be smaller than the lattice constant $a \approx 0.38$ nm in obvious conflict with the well-known Joffe-Regel limit $l \geq a$.^{29,30} In other words the maximal intrinsic resistivity is given by $\rho_0^{\text{max}} [\text{m}\Omega\text{cm}] \approx 1.3v_F [10^7 \text{ cm/s}] / (\hbar\omega_{\text{pl}} [\text{eV}])^2 = 0.29$ m Ω cm in the ISB dirty limit. Such resistivities (0.33 m Ω cm) have been reported in most heavily (neutron) irradiated samples by Karkin et al.³¹

B. Specific heat in the normal state

In order to describe the specific heat data in the normal state in an extended temperature range $T_c < T < 30$ K, the Debye low temperature limit approximation for the lattice contribution (see Eq. (3)) was replaced by

$$c_{\text{lattice}}(T) = c_D(T) + c_E(T).$$

Here,

$$c_D(T) = \sum_{i=1}^3 3R \left(\frac{T}{\Theta_{D_i}} \right)^3 \int_0^{\Theta_{D_i}/T} dx \frac{e^x x^4}{(e^x - 1)^2}$$

stands for the Debye model^{32,33} describing the 3 acoustic phonon branches, whereas the Einstein model^{32,33}

$$c_E(T) = \sum_{i=4}^{15} R \left(\frac{\Theta_{E_i}}{T} \right)^2 \frac{\exp(\Theta_{E_i}/T)}{[\exp(\Theta_{E_i}/T) - 1]^2}$$

describes the 12 optical branches.

We found that the 9 energetically lowest phonons (3 acoustic and 6 optical modes) are sufficient to describe the normal state specific heat up to $T = 30$ K. The result of the fit is shown in Fig. 9. The Sommerfeld parameter converged to $\gamma_N^* = 31.4$ mJ/molK², greater than determined from Fig. 5. Specific heat measurements up to $T = 300$ K on another piece from the initially prepared sample (which are not presented here) give the remaining 6 optical mode temperatures. The obtained Debye and Einstein temperatures and the belonging grouping

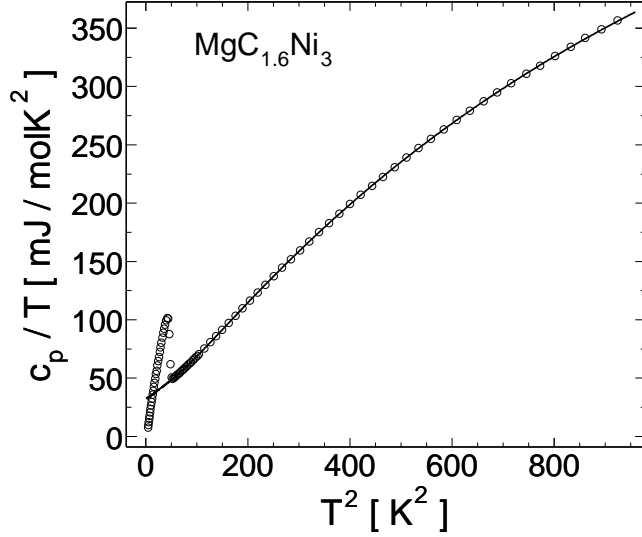


FIG. 9: Specific heat data $c_p(T)/T$ vs. T^2 for zero magnetic field in the temperature range up to 30 K. The solid line is a fit of the lattice model (see text for details), showing very good agreement with the data for $T_c < T < 30$ K.

parameters ν_i are summarized in Tab. I. The phonon energies are in good agreement with recent calculations.²²

The corresponding phonon spectrum has the form³³

$$F_{\text{ph}}(\omega) = 3\omega^2 \left[\nu_{\text{D1}} \frac{\theta(\Omega_{\text{D1}} - \omega)}{\Omega_{\text{D1}}^3} + \nu_{\text{D2}} \frac{\theta(\Omega_{\text{D2}} - \omega)}{\Omega_{\text{D2}}^3} \right] + \sum_{i=1}^5 \frac{\nu_{\text{E}i}}{\sqrt{2\pi\sigma_i^2}} \exp \left[-\frac{(\omega - \Omega_{\text{E}i})^2}{2\sigma_i^2} \right],$$

where $\theta(x)$ is the well known step-function and Ω denotes the corresponding cut-off temperatures in meV. The result including higher optical modes is shown in Fig. 10. Our model parameters even reproduce the rather complex phonon dispersion along the Γ -X direction in the first Brillouin zone at low phonon energies, as can be seen from Fig. 11, where the used model is compared with calculations reported by Ignatov et al.²² Even though our model only involves constant and linear dispersion by the Einstein and Debye model, respectively, the calculated phonon dispersion (right panel) is well reproduced (left panel), by means of superpositions of acoustic and optic phonon modes. The high-energy optic phonons obtained from the model are shifted to lower energies than predicted by the calculations. The shift is most probably caused by anharmonic effects, which usually increase specific heat data at higher temperatures.²²

To investigate the electron-phonon coupling strength, the electron-phonon interaction function $\alpha^2 F_{\text{ph}}(\omega)$ is of interest. The coupling function $\alpha^2(\omega)$ is usually extracted from tunneling measurements. In the case of A15 compounds³⁴ and some borocarbides,³⁵ $\alpha^2(\omega)$ is found to be of the form $\alpha^2(\omega) = \delta/\sqrt{\omega}$, with a scaling parameter δ .

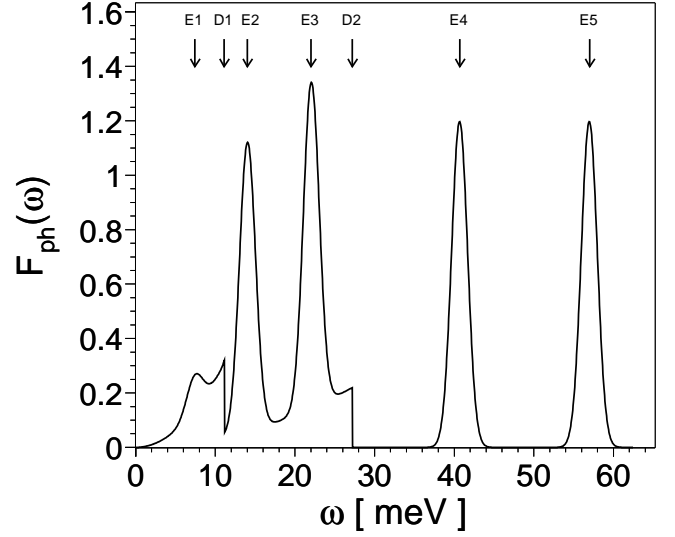


FIG. 10: Schematic phonon model spectrum $F_{\text{ph}}(\omega)$ for $\text{MgC}_{1.6}\text{Ni}_3$ derived from fit parameters according to Tab. I. The peak width of the optical modes was chosen arbitrarily as $\sigma_i^2 = 1$.

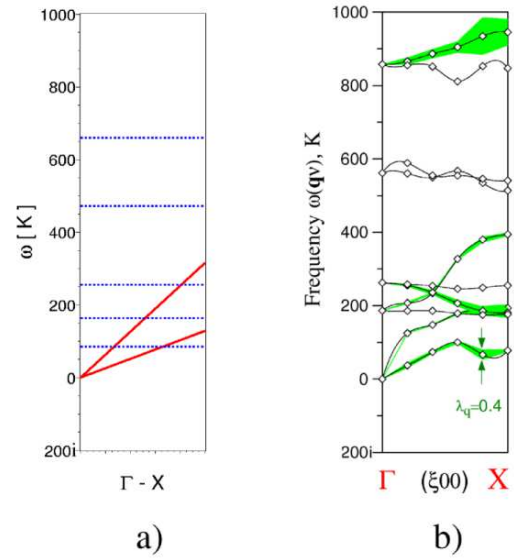


FIG. 11: Phonon dispersion along Γ -X direction in the first Brillouin zone. a) Our model with acoustic phonons (black lines) and optic phonons (dashed lines) according to Tab. I, b) Calculations reported by Ignatov et al. after Ref. 22.

Within this approach the logarithmically averaged mean phonon frequency ω_{ln} was determined from

$$\omega_{\text{ln}} = \exp \left(\frac{2}{\lambda_{\text{ph}}} \int_0^\infty d\omega \frac{\alpha^2(\omega) F(\omega)}{\omega} \ln \omega \right),$$

$$\lambda_{\text{ph}} = 2 \int_0^\infty d\omega \frac{\alpha^2(\omega) F(\omega)}{\omega} \quad (5)$$

as $\omega_{\text{ln}} = 143$ K. This frequency is used in the well known

McMillan formula (refined by Allen and Dynes)³⁶

$$T_c \approx \frac{\omega_{\text{ln}}}{1.2} \exp \left[-\frac{1 + \lambda_{\text{ph}}}{\lambda_{\text{ph}} - \mu^* (1 + 0.6\lambda_{\text{ph}})} \right] \quad (6)$$

to estimate the electron-phonon coupling constant λ_{ph} . μ^* denotes the usually weak Coulomb pseudopotential which has been chosen as $\mu^* = 0.13$ in this case. With $T_c = 6.8$ K the electron-phonon coupling constant amounts $\lambda_{\text{ph}} = 0.84$, suggesting moderate coupling as proposed, for instance in Refs. 1 and 15. However, the low value of λ_{ph} estimated from Eq. (6) is in contradiction with our specific heat data as already mentioned in Sec. IV B. In particular, $\lambda_{\text{ph}} = 1.45$ was derived from the ratio γ_N^*/γ_0 and also the high value of the superconducting jump $\Delta c(T_c)/(\gamma_N T_c) = 2.09$ indicates strong electron-phonon coupling. Strong electron-phonon coupling was also predicted by Ignatov et al.²² ($\lambda_{\text{ph}} = 1.51$) on the base of the calculations mentioned above.

In this context a more precise analysis of the low temperature normal state specific heat data is required. As can be seen from the dashed line in Fig. 12, the extended lattice model does not describe the magnetic field data. Even larger deviations are observed if the experimental data are described within the low temperature limit of the Debye model (see Fig. 5). Lin et al.¹⁵ who found a similar upturn of the experimental data at low temperatures tried to explain this behavior by the presence of Ni impurities. However, our x-ray analysis (see Fig. 3) shows no indication for Ni impurities in our sample. Recently, Shan et al.¹⁶ found that the mentioned upturn can be easily reduced by lowering the carbon content. They attributed the observed upturn to some kind of boson mediated electron-electron interactions in MgC_xNi_3 . This argument motivated us to search for other possible sources to explain the low temperature upturn of the normal state specific heat data.

The easiest explanation is an additional electron-boson interaction which may be an

1. electron-phonon interaction originating from additional phonon-softening of the lowest acoustic mode (suggested by Ignatov et al.²² and verified experimentally by Heid et al.³⁷) and / or
2. electron-paramagnon interaction (see Sec. I).

Specific heat measurements let not clearly distinguish between these possible origins, but since magnetization measurements on our sample (not presented here) show increasing spin fluctuations below ~ 30 K in accord with previous statements (see Sec. I), the focus in this paper lies on the electron-paramagnon interaction scenario. This is additionally supported by a small magnetic field dependence of the specific heat data, typically found in the presence of ferromagnetic spin fluctuations.

Within Eliashberg theory the renormalized normal state specific heat is described by the temperature dependent thermal mass $\Delta m^*(T)/m_{\text{band}}$. Its contribution

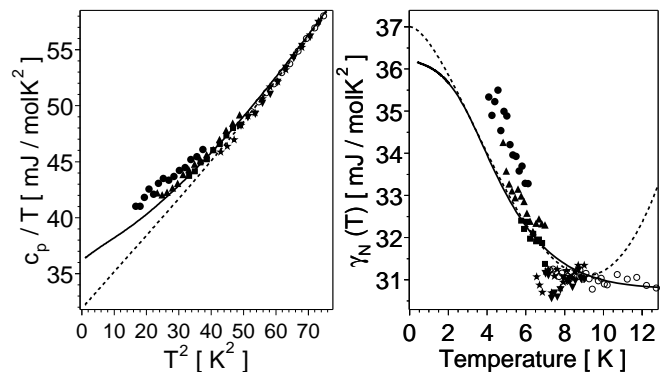


FIG. 12: Low temperature normal state total and electronic specific heat including field measurements (0.5 T (\blacktriangledown), 2 T (\star), 4 T (\blacksquare), 6 T (\blacktriangle) and 8 T (\bullet)). Left panel: Specific heat data $c_p(T)/T$ vs. T^2 . Dotted line: Extended lattice model describing the zero field data (see Fig. 9). Solid line: Fit of the model (including lattice and paramagnon contribution) to the data. Right panel: electronic specific heat $\gamma_N(T)$ vs. T in the normal state. Black line: Sommerfeld parameter $\gamma_N(T)$ of the model (see text for details), describing the observed upturn of the specific heat at low temperatures. Dotted line: Qualitative model for spin fluctuations according to Eq. (8).

to the specific heat is given by

$$\Delta\gamma_{\text{sf}}(T) = \frac{\Delta m^*(T)}{m_{\text{band}}} \gamma_0,$$

with³⁸

$$\frac{\Delta m^*(T)}{m_{\text{band}}} = \frac{6}{\pi k_{\text{B}} T} \int_0^\infty d\omega \alpha^2 F(\omega) \left\{ -z - 2z^2 \text{Im}[\psi'(iz)] - z^3 \text{Re}[\psi''(iz)] \right\},$$

where $\psi(iz)$ is the digamma function and $z = \omega/(2\pi k_{\text{B}} T)$. The additional electron-paramagnon interaction function is of the form

$$\alpha^2 F_{\text{sf}} = a\omega\theta(\Omega_{\text{P}} - \omega) + \frac{b}{\omega^3}\theta(\omega - \Omega_{\text{P}}). \quad (7)$$

A corresponding fit results in a paramagnon-model temperature of $\Omega_{\text{P}} \approx 2.15$ meV $\Rightarrow \Theta_{\text{P}} \approx 25$ K with a thermal mass of $\Delta m^*(T = 0 \text{ K})/m \approx 0.43$, which is of the same order of magnitude as determined by Shan et al.¹⁶. Since this low energy excitation concerns the electronic part of the specific heat, we add it to the Sommerfeld parameter which then becomes temperature dependent. The electronic contribution to the specific heat increases from initially $\gamma_N^* = 31.4$ mJ/molK² to $\gamma_N(0) = 36.0$ mJ/molK². This is understandable since the paramagnon interaction dominates in the temperature range below 10 K. The black line in Fig. 12 shows the good agreement of this extended model with the experimental data in the low temperature region. The magnetic field dependence of

the paramagnons (which in addition can be temperature-dependent) is not included in the model. In the following $\gamma_N(T)$ is denoted as γ_N for the sake of simplicity.

The usually applied model

$$\gamma_N \propto \delta T^2 \ln(T/T_0), \quad (8)$$

to describe spin fluctuation behavior is shown in the right panel of Fig. 12 for comparison.

At this point the question of the strength of the coupling may be rechecked. Including the additional electron-paramagnon interaction, the Allen-Dynes formula Eq. (6) becomes

$$T_c \approx \frac{\omega_{ln}}{1.2} \exp \left[-\frac{1 + \lambda}{\lambda_{ph} - \lambda_{sf} - \mu^* (1 + 0.6\lambda_{ph})} \right], \quad (9)$$

with $\lambda = \lambda_{ph} + \lambda_{sf}$. Using $\omega_{ln} = 143$ K, $T_c = 6.8$ K, $\mu^* = 0.13$ and $\lambda_{sf} = 0.43$, the electron-phonon coupling constant rises to $\lambda_{ph} = 1.85$. Using this value, the electron-phonon interaction function based on the approach $\alpha(\omega) = \delta/\sqrt{\omega}$ can now be determined by scaling the factor δ according to Eq. (5). The electron-boson interaction functions $\alpha^2 F_{ph}(\omega)$ and $\alpha^2 F_{sf}(\omega)$ are shown in Fig. 13.

The reliability of the model approach for the electron-phonon coupling function $\alpha(\omega) = \delta/\sqrt{\omega}$ can directly be checked from the band structure, using the ratio between the Sommerfeld parameter $\gamma_N(0) = 36.0$ mJ/molK² and the free electron parameter $\gamma_0 = \pi^2 k_B^2 N(E_F)/3 = 11.0$ mJ/molK²,

$$\frac{\gamma_N(0)}{\gamma_0} = (1 + \lambda_{ph} + \lambda_{sf}). \quad (10)$$

With $\lambda_{sf} \approx 0.43$, the electron-phonon coupling constant becomes $\lambda_{ph} \approx 1.9$, showing very good agreement between both approaches.

In the next section, the analysis of the specific heat in the normal state will be extended to the superconducting state.

C. Specific heat in the superconducting state

Fig. 14 shows the superconducting part of the electronic specific heat $\Delta c(T) = c_p(T) - c_n(T)$, obtained from the zero-field data. The superconducting transition temperature $T_c = 6.8$ K has been estimated by an entropy conserving construction (dashed line in Fig. 14). This value agrees well with the transition temperatures $T_c = 6.9$ K and $T_c = 7.0$ K, derived from resistance and from ac susceptibility data, respectively. The conservation of entropy, $\Delta S(T) = \int_0^{T_c} (\Delta c/T) dT$, is shown in the inset of Fig. 14. It was already mentioned, that the high value of the jump $\Delta c(T_c)/(\gamma_N T_c) = 2.09$ found for the investigated sample can be explained by strong electron-phonon coupling. Nevertheless, we will start to analyze $\Delta c(T)$ for $T < T_c/2$ within the BCS theory, since the deviation from the weak-coupling temperature dependence

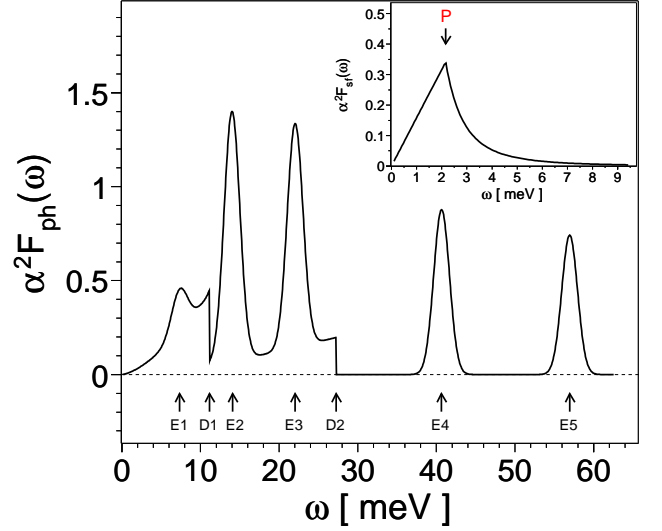


FIG. 13: Electron-phonon interaction function $\alpha^2 F_{ph}(\omega)$ for MgC_{1.6}Ni₃. Phonon energies are marked by “E*i*”, respectively “D*i*” (see Fig. 10 and Tab. I). Inset: Electron-paramagnon interaction function $\alpha^2 F_{sf}(\omega)$ according to Eq. (7), the paramagnon energy is marked by “P”.

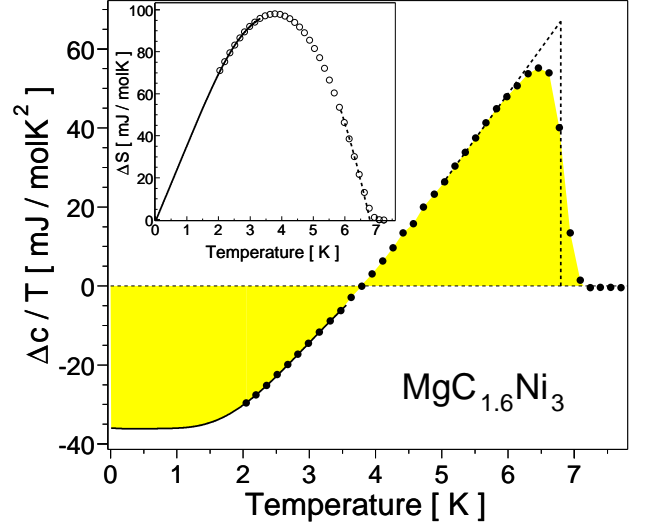


FIG. 14: Electronic specific heat data $\Delta c/T$ vs. T in the superconducting state (filled circles). The solid line in the temperature range $0 < T < 3.4$ K corresponds to Eq. (11). Dotted line: Entropy conserving construction to get the idealized jump. Inset: Entropy conservation for the electronic specific heat in the temperature range $0 < T < T_c$.

of the gap is mainly restricted to the vicinity of the jump. The temperature dependence of $\Delta c(T) = c_p(T) - c_n(T)$ in the weak-coupling BCS theory ($T_c \ll \omega_{ln}$) is given by

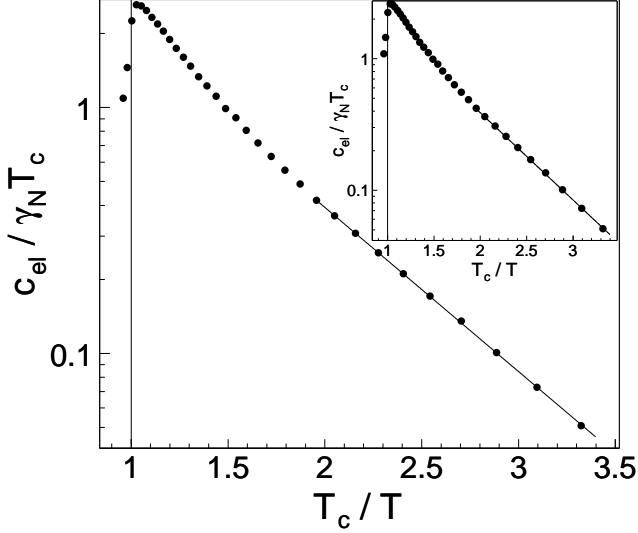


FIG. 15: Normalized electronic specific heat contribution vs. T_c/T . The black line is a fit of Eq. (12) to the experimental data. The inset shows a fit of the two-band approximation given by Eq. (13).

an approximative formula

$$\Delta c(T) = 8.5\gamma_N T_c \exp\left(-0.82\frac{\Delta_{\text{BCS}}(0)}{k_B T}\right) - \gamma_N T, \quad (11)$$

valid in the temperature range of $2 < T_c/T < 6$ corresponding in this case to $1 \text{ K} < T < 3.4 \text{ K}$. Eq. (11) can be fitted to the data by using the phenomenological gap $2\Delta_{\text{exp}}/k_B T_c = 3.75$, slightly exceeding the BCS weak coupling prediction $2\Delta_{\text{BCS}}(0)/k_B T_c = 3.52$. The fit, which is shown as black line in Fig. 14, describes the experimental data in the range of $2 \text{ K} < T < 3.5 \text{ K}$ quite well.

To examine the temperature dependence of the electronic specific heat at

$$\begin{aligned} c_{\text{el}} &= c_p(T) - c_{\text{lattice}}(T) \\ &= \Delta c(T) + \gamma_N T_c \end{aligned}$$

at $H = 0$ in detail, $c_{\text{el}}(T)/\gamma_N T_c$ is plotted logarithmically vs. T_c/T (Fig. 15). The corresponding formula to Eq. (11) reads

$$\frac{c_{\text{el}}(T)}{\gamma_N T_c} = 8.5 \exp\left(-0.82\frac{\Delta_{\text{exp}}}{k_B T}\right), \quad (12)$$

if $\Delta_{\text{BCS}}(0)$ is replaced by Δ_{exp} . The black line in Fig. 15 is a fit of Eq. (12) to the experimental data, which show an exponential temperature dependence at low temperatures ($T_c/T \geq 2$). This is a strong indication for s -wave superconductivity in $\text{MgC}_{1.6}\text{Ni}_3$. A natural explanation for the discrepancy from the expected BCS gap value of $2\Delta_{\text{BCS}}(0)/k_B T_c = 3.52$ to the experimentally found $2\Delta_{\text{exp}}/k_B T_c = 3.75$ emerges from

1. the two-band character of $\text{MgC}_{1.6}\text{Ni}_3$ and
2. the enhanced electron-phonon coupling.

The electronic specific heat can be analyzed within a two-gap model, simply by extending Eq. (12) with a second gap

$$\begin{aligned} \frac{c_{\text{el}}(T)}{\gamma_N T_c} &= 8.5 \left[0.85 \exp\left(-0.82\frac{\Delta_1}{k_B T}\right) \right. \\ &\quad \left. + 0.15 \exp\left(-0.82\frac{\Delta_2}{k_B T}\right) \right], \quad (13) \end{aligned}$$

using 85 % contribution for the hole band and 15 % contribution for the electron band. The dotted line in Fig. 15 shows this fit for two gaps with $2\Delta_1/k_B T_c = 3.67$ (fitted parameter) and $2\Delta_2/k_B T_c = 4.50$ (fixed parameter). This situation is nearly indistinguishable from the single band model (see inset of Fig. 15). The two-gap model is of considerable interest, since in this case the large gap found in recent tunneling measurements of Ref. 13 ($2\Delta/k_B T_c = 4.6$) and Ref. 17 ($2\Delta/k_B T_c = 4.3$) is reproduced.

Even the lower gap of the two-gap model exceeds the BCS weak-coupling limit. This and the strongly enhanced specific heat jump $\Delta c(T_c)$ are clear indications of strong electron-phonon coupling in accordance with our normal state specific heat analysis. Thus it is now straightforward to investigate the electron-phonon coupling strength and thus, the characteristic phonon frequency ω_{ln} , introduced in Sec. VB, from the superconducting state characteristics. The Eliashberg theory provides the following approximate formulas, which include strong coupling corrections within an isotropic single band model and links $x = \omega_{\text{ln}}/T_c$ to experimental thermodynamic quantities:²⁰

$$\frac{2\Delta(0)}{k_B T_c} = 3.53B_0(x), \quad (14a)$$

$$\frac{\Delta c(T_c)}{\gamma_N T_c} = 1.43B_1(x), \quad (14b)$$

$$\frac{\Delta c(T) - \Delta c(T_c)}{\gamma_N T_c - \gamma_N T} = -3.77B_2(x), \quad (14c)$$

$$\frac{\gamma_N T_c^2}{H_c^2(0)} = 0.168B_3(x), \quad (14d)$$

$$\frac{H_c(0)}{\frac{dH_c}{dT}\big|_{T_c} T_c} = 0.576B_4(x). \quad (14e)$$

The corresponding logarithmic correction terms are given by

$$B_0(x) = 1 + 12.5x^{-2} \ln \frac{x}{2}, \quad (15a)$$

$$B_1(x) = 1 + 53x^{-2} \ln \frac{x}{3}, \quad (15b)$$

$$B_2(x) = 1 + 117x^{-2} \ln \frac{x}{2.9}, \quad (15c)$$

$$B_3(x) = 1 - 12.2x^{-2} \ln \frac{x}{3}, \quad (15d)$$

$$B_4(x) = 1 - 13.4x^{-2} \ln \frac{x}{3.5}. \quad (15e)$$

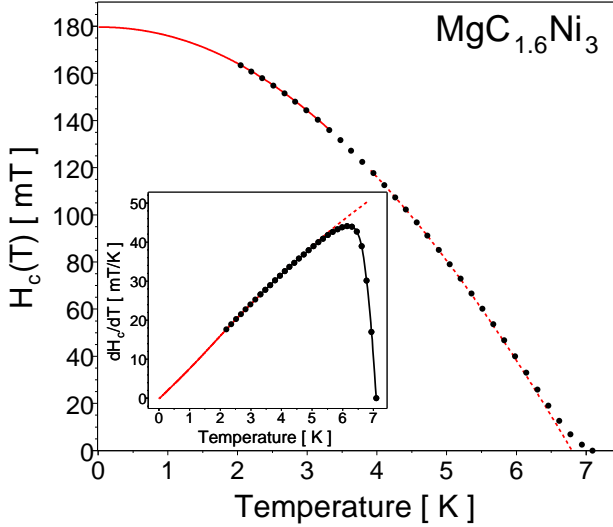


FIG. 16: Temperature dependence of the thermodynamic critical field $H_c(T)$ (filled circles) derived from the electronic specific heat in the superconducting state using Eq. (16). Solid line ($0 < T < 3.4$ K): Single band model according to Eq. (12). Dotted line: Idealized jump construction (see Fig. 15). Inset: Derivative dH_c/dT vs. T (filled circles) and idealized jump (dotted line).

Now, using Eq. (14a), $T_c = 6.8$ K and the gap value $\Delta_{\text{exp}}(2 \text{ K}) = 1.10 \text{ meV}$, one arrives at $\omega_{\text{ln}} = 149$ K.

Using the value of the idealized jump of the specific heat, $\Delta c(T_c)/(\gamma_N T_c) = 2.09$ in Eq. (14b) with $T_c = 6.8$ K, $\omega_{\text{ln}} = 88$ K is derived.

Comparing the linear slope of the idealized specific heat in the superconducting state of -6.7 , obtained from Fig. 14 with Eq. (14c), one gets $\omega_{\text{ln}} = 109$ K.

In view of strong-coupling effects the ratio $\gamma_N T_c^2/H_c^2(0)$, implying again only thermodynamic quantities, is of interest. Known superconductors show values between $0.17 \dots 0.12$ ranging from weak to strong coupling, respectively (see for example page 1086 of Ref. 20). The thermodynamic critical field $H_c(T)$ can be determined with the help of the Gibbs free energy $dF = -SdT - MdB$ as

$$H_c(T) = \sqrt{-8\pi\Delta F}. \quad (16)$$

ΔF is to be extracted from the specific heat in the superconducting state, $\Delta c(T) = -Td^2(\Delta F)/dT^2$. The temperature dependence of $H_c(T)$ is shown in Fig. 16. With $H_c(0) = 179.6 \text{ mT}$ we found $\gamma_N T_c^2/H_c^2(0) = 0.155$. From Eq. (14d) we get $\omega_{\text{ln}} = 110$ K (with $T_c = 6.8$ K).

Next, from the derivative of the thermodynamic critical field at zero temperature, dH_c/dT the ratio $H_c(0)/(dH_c(T)/dT|_{T_c} T_c)$ can be estimated. The value at $T = T_c$ (of the idealized jump construction), amounts $dH_c(T)/dT|_{T_c} = 50.236$ (see dashed line in the inset of Fig. 16). Using the experimental value of

$H_c(0)/(dH_c(T)/dT|_{T_c} T_c) = 0.525$ in Eq. (14e), a value of $\omega_{\text{ln}} = 102$ K is extracted.

It should be noted that Eqs. (14a) and (14e) can be used to estimate the value of the gap $\Delta(0)$ from the thermodynamic critical field $H_c(0)$, due to similar dependences on strong coupling corrections:³⁹

$$\left(\frac{T}{H_c(0)} \frac{dH_c(T)}{dT} \right) \Big|_{T=T_c} \approx \frac{\Delta(0)}{k_B T_c}.$$

Using $dH_c(T)/dT|_{T_c} = 50.236$, we get $2\Delta(0)/k_B T_c \approx 3.80$, agreeing well with the single band result $2\Delta_{\text{exp}}/k_B T_c = 3.75$ of Eq. (12).

In summary, ω_{ln} was estimated from five different thermodynamic relations, only involving experimental results. The mean value $\overline{\omega_{\text{ln}}} = (111 \pm 23)$ K is in good agreement with calculations of Ignatov et al.²² An overview of the results is given in Fig. 17. Note, that a similar analysis was already successfully used to describe some borocarbide superconductors.^{35,40}

The mean value $\overline{\omega_{\text{ln}}}$, derived from the superconducting state is somewhat smaller than the normal state result, $\omega_{\text{ln}} = 143$ K. This may be attributed to an additional phonon softening contribution or the approximative approach of the electron-phonon coupling function $\alpha^2(\omega)$ (see Sec. VB). Nevertheless by checking Eq. (9) with $\overline{\omega_{\text{ln}}} = (111 \pm 23)$ K, $T_c = 6.8$ K, $\mu^* = 0.13$ and $\lambda_{\text{sf}} = 0.43$ the electron-phonon coupling constant becomes $\lambda_{\text{ph}} = 1.9 \dots 2.3$, whereas $\lambda_{\text{ph}} = 1.85$ was derived from $\omega_{\text{ln}} = 143$ K for the same parameters. It should be noted here, that Eqs. (14) were derived assuming a small value for the Coulomb pseudopotential μ^* , which is oversimplified considering enhanced electron-paramagnon coupling found in this analysis. A rough correction would shift the characteristic phonon frequency ω_{ln} to slightly higher values and a coupling constant of $\lambda_{\text{ph}} \approx 1.9$ seems to be most likely. Note that a similar analysis was already successfully used to describe some borocarbide superconductors.^{35,40}

The analysis of the thermodynamic properties of $\text{MgC}_{1.6}\text{Ni}_3$ presented so far clearly points to strong electron-phonon coupling. However, the temperature dependence of the thermodynamic critical field $H_c(T)$ shown in Fig. 16 strongly deviates from analogous data for well-known strong coupling superconductors such as Hg or Pb. $H_c(T)$ is usually analyzed in terms of the deviation function $D(t) = H_c(T) = H_c(0)(1 - t^2)$ with $t = T/T_c$. The deviation function of the above mentioned strong coupling superconductors is positive and goes through a maximum at $t^2 \approx 0.5$. The deviation function of $\text{MgC}_{1.6}\text{Ni}_3$ is shown in Fig. 18. Instead of the expected positive sign, $D(t^2)$ of $\text{MgC}_{1.6}\text{Ni}_3$ becomes negative already above about $0.3T_c$. The shape of the deviation function of $\text{MgC}_{1.6}\text{Ni}_3$ closely resembles that one of Nb having an electron-phonon coupling strength of $\lambda_{\text{ph}} \approx 1.0$. We remind the reader that the weak coupling BCS model yields a negative maximum deviation of $\approx 3.8\%$ (see Fig. 18). Thus, at first glance, our result seems to be in contradiction with the strong electron-phonon coupling suggested

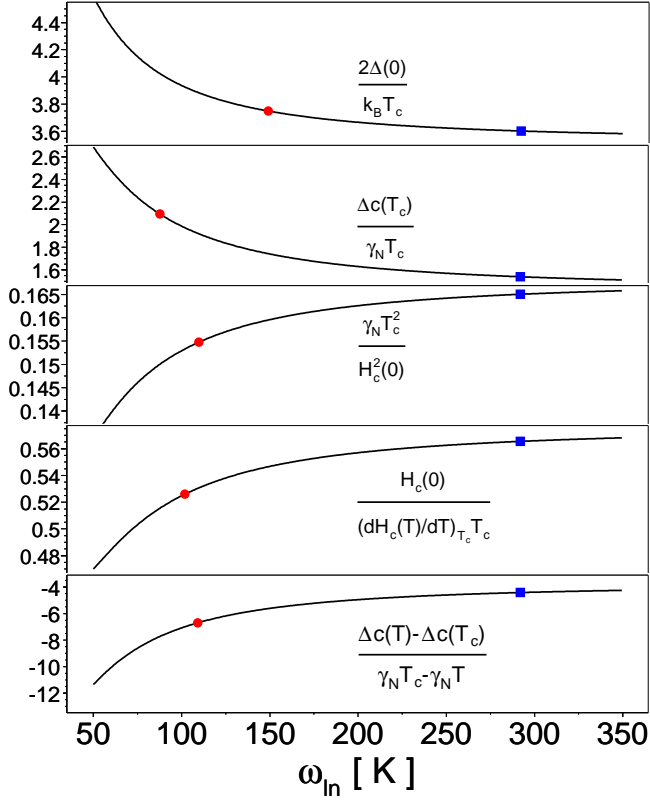


FIG. 17: Several thermodynamic quantities in dependence on the characteristic phonon frequency ω_{in} according to Eqs. (14) and (15). Filled circles: thermodynamic quantities estimated for $\text{MgC}_{1.6}\text{Ni}_3$ from experimental data. Strong discrepancies are found within the low temperature Debye limit (filled squares). Note that the weak-coupling limit is reached in the asymptotic extrapolation $\omega_{\text{in}} \rightarrow \infty$.

above. It turns out that this contradiction can be resolved, taking into account a splitting of the electron-phonon interaction function in a high and a low (soft) energy part. This is illustrated in Fig. 19, where a two phonon peak spectrum with equal coupling strengths of both peaks located at ω_1 and ω_2 has been analyzed in the strong coupling case of $\lambda_{\text{ph}} \approx 2$ under consideration. The theoretical curves calculated within the ISB are shown for different frequency ratios ω_1/ω_2 . For $\omega_1/\omega_2 \approx 8$, the “standard” strong coupling behavior, namely a positive deviation function, is completely removed and the deviation function becomes negative. Considering the low energy modes E1 and D1, found in the analysis of the specific heat in the normal state (see Figs. 10 and 13), this situation is easily imaginable to be valid in the case of MgCNi_3 .

In the superconducting state a linear-in- T electronic specific heat contribution $\gamma(H)T$ arises from the normal conducting cores of the flux lines for applied magnetic fields $H > H_{c1}$.

This contribution can be expressed as $\gamma(H)T = c_p(T, H) - c_p(T, 0)$,⁴² where $c_p(T, 0)$ is the specific heat

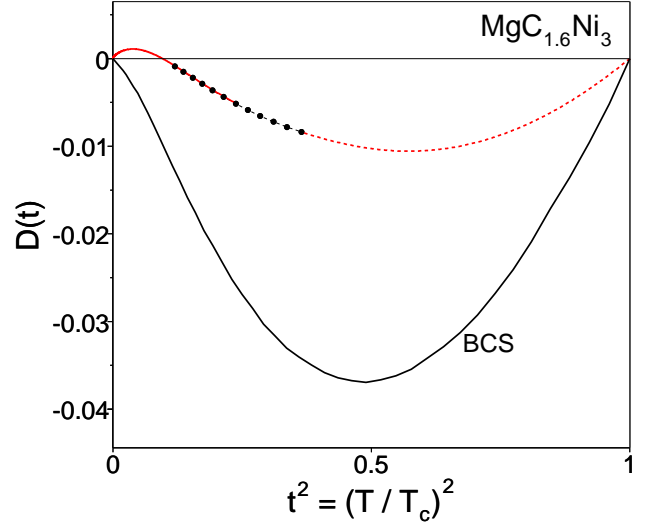


FIG. 18: Deviation function of the thermodynamic critical field of $\text{MgC}_{1.6}\text{Ni}_3$ (filled circles) as function of $(T/T_c)^2$. The solid line for $0 < T < 0.34$ K corresponds to Eq. (12), the dotted line corresponds to the idealized jump construction (see Fig. 14). For comparison, the weak coupling BCS result⁴¹ is shown.

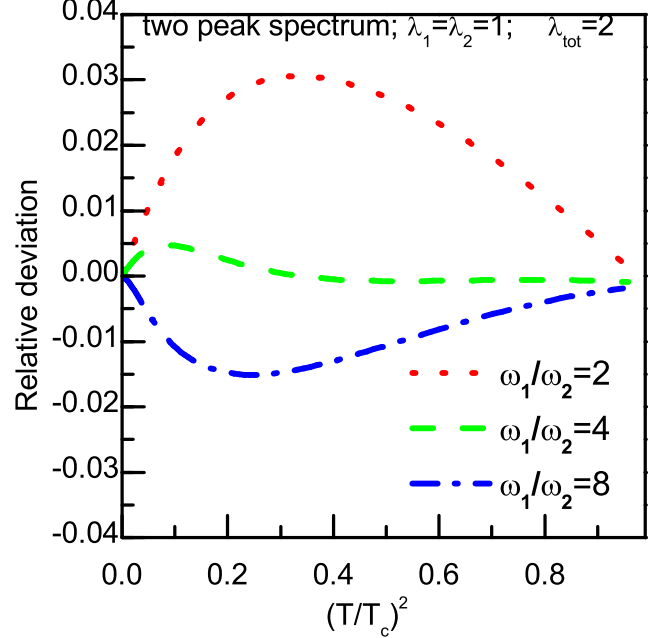


FIG. 19: Normalized deviation function calculated within the Eliashberg theory for an idealized two-peak phonon spectrum located at ω_1 and ω_2 with equal electron-phonon coupling parameters $\lambda_1 = \lambda_2 = 1$ and strong total coupling parameter of $\lambda_{\text{ph,tot}} = 2$. Shown are results for $\omega_1/\omega_2 = 2, 4$ and 8 .

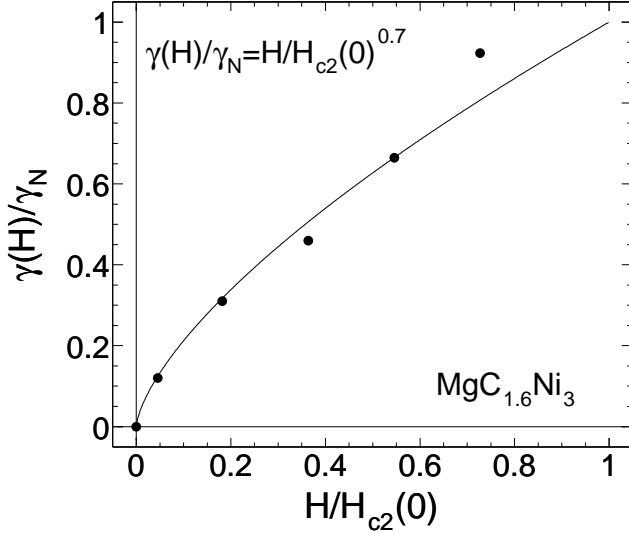


FIG. 20: Normalized field-dependent Sommerfeld parameter $\gamma(H)/\gamma_N$ plotted against $H/H_{c2}(0)$. Filled circles: $\gamma(H)/\gamma_N = [c_p(T, H) - c_p(T, 0)]/\gamma_N$ at $T = 2$ K for different applied magnetic fields. The black line is a fit of $\gamma(H)/\gamma_N = (H/H_{c2}(0))^{0.7}$ using $H_{c2}(0) = 11$ T and γ_N at $T = 2$ K.

in the Meissner state. Specific heat data for $\text{MgC}_{1.6}\text{Ni}_3$ at $T = 2$ K were analyzed in order to derive the field dependence of $\gamma(H)$. In Fig. 20, the obtained $\gamma(H)/\gamma_N$ is plotted against $H/H_{c2}(0)$ using $H_{c2}(0) = 11.0$ T.

The field data of c_p/T shown in Fig. 20 can be described in accord with results from Ref. 15 by the expression $\gamma/\gamma_N = (H/H_{c2}(0))^{0.7}$ which differs from the linear $\gamma(H)$ law expected for isotropic s -wave superconductors in the dirty limit.

A non-linear field dependence close to $\gamma(H) \propto H^{0.5}$ has been reported for some unconventional superconductors with gap nodes in the quasiparticle spectrum of the vortex state as $\text{YBa}_2\text{Cu}_3\text{O}_7$,⁴³ and in the heavy fermion superconductor UPt_3 ,⁴⁴ but also in some clean s -wave superconductors as CeRu_2 ,⁴⁵ NbSe_2 ,^{42,46} and the borocarbides $\text{RNi}_2\text{B}_2\text{C}$ ($R = \text{Y, Lu}$).^{47,48} Delocalized quasiparticle states around the vortex cores, similar as in d -wave superconductors, seem to be responsible for the non-linear $\gamma(H)$ dependence in the borocarbides.^{49,50}

D. The main superconducting and thermodynamic parameters

In this subsection we collect the values of the main physical parameters we have found experimentally and compare them with available data in the literature. In order to make this comparison as complete as possible we estimate (calculate), from our data and from those of Ref. 13, the lower critical field $H_{c1}(0)$ and the penetration depth $\lambda_L(0)$ at zero temperature adopting the applicability of the standard Ginzburg-Landau (GL) theory.

TABLE II: Main superconducting and thermodynamic electronic parameters for MgCNi_3 .

		Present work ^a	Ref. 51 ^a	Ref. 13 ^b	Ref. 52 ^b
T_c	[K]	6.8	6.4	7.63	7.3
$H_{c2}(0)$	[T]	11	11.5	14.4	16
$H_c(0)$	[T]	0.18	0.29 ± 0.04	0.19	0.6
$H_{c1}(0)$	[mT]	11.3 ^c	23 ± 7 ^c	10.0 ^c	12.6 ^d
$\xi_{\text{GL}}(0)$	[nm]	5.47	5.4	4.6	4.5
$\kappa(0)$		43.3	29.0 ± 5.0	54.0	51
$\lambda_L(0)$	[nm]	237. ^c	154 ± 26 ^d	248. ^c	230.0 ^c
γ_N	$[\frac{\text{mJ}}{\text{molK}^2}]$	31.4	33.6	30.1	
$\frac{\Delta_c}{\gamma_N T_c}$		2.09	1.97	2.1	
Θ_D^*	[K]	292	287	284	
ω_{ln}	[K]	143	135. ^e	161. ^e	

^aUsing a parabolically extrapolated $H_{c2}(0)$ value.

^bUsing the artificial WHH estimate for $H_{c2}(0)$.

^cCalculated.

^dMeasured.

^eCalculated (Eq. (9) using $\lambda_{\text{ph}} = 1.85$, $\lambda_{\text{sf}} = 0.43$, $\mu^* = 0.13$).

Within this theory the penetration depth is given by the relation

$$\lambda_L(0) = \kappa(0)\xi_{\text{GL}}(0), \quad (17)$$

where the Ginzburg-Landau coherence length $\xi_{\text{GL}}(0)$ and the Ginzburg-Landau parameter κ are related to the upper and the thermodynamic critical fields as:

$$\xi_{\text{GL}}(0) = \sqrt{\Phi_0/2\pi H_{c2}(0)},$$

$$\kappa(0) = \frac{H_{c2}(0)}{\sqrt{2}H_c(0)},$$

with the flux quantum Φ_0 . With $H_{c2}(0) = 11$ T and $H_c(0) = 180$ mT (see Sec. V C), $\xi_{\text{GL}}(0) = 5.47$ nm and $\kappa(0) = 43.3$ are obtained. Using these values in Eq. (17), the penetration depth is estimated to be $\lambda_L(0) = 237$ nm. Our calculated value agrees well with measurements performed by Prozorov et al.¹⁸ resulting $\lambda_L(0) = (250 \pm 20)$ nm. It should be noted that Lin et al.¹⁵ measured a penetration depth of $\lambda_L(0) = (128 \dots 180)$ nm for their sample (see also Ref. 51), possible consequences will be discussed in Sec. VIA. To complete the critical field analysis, the lower critical field $H_{c1}(0)$ can be estimated using

$$H_{c1}(0)H_{c2}(0) = H_c^2(0) (\ln \kappa(0) + 0.08).$$

With $H_{c2}(0) = 11$ T and $\kappa(0) = 43.3$ we get $H_{c1}(0) = 11.3$ mT, agreeing well with $H_{c1}(0) = 12.6$ mT, measured by Jin et al.⁵² The results are shown in Tab. II, where for comparison result of Refs. 13, 51 and 52 have been included. Comparing these sets one finds a general qualitative accord.

VI. THEORETICAL ANALYSIS AND DISCUSSION

Naturally, the obtained parameter set is model dependent. In this context even the case of relatively simple Fermi surfaces provides a difficult task to solve the full three(four)-dimensional Eliashberg problem with given $v_F(\vec{k})$ and $\alpha^2 F(\vec{k}, \vec{k}', \omega)$ for all physical quantities of interest. However, the solution of this problem can be sufficiently simplified for three practically important cases:

1. the relatively simple standard isotropic single band model (ISB), where $v_F(\vec{k})$ is constant and the spectral function $\alpha^2 F$ depends only on the boson (phonon) frequency,
2. a separable anisotropic single band model which exploits the so called first order Fermi surface harmonic approximation and
3. the isotropic two-band model (ITB). The latter is a straightforward generalization of the ISB with respect to two order parameters.

Due to the present lack of single crystal samples we will ignore the second issue. In addition, the cubic structure of MgCNi₃ suggests only weak anisotropy effects.

A. The isotropic single band analysis

In the following section the electron-phonon coupling strength λ_{ph} is extracted from a simultaneous analysis of the upper critical field and the penetration depth in terms of the unknown impurity scattering rate γ_{imp} [K]. Since the specific heat measurements do not clearly characterize MgCNi₃ as a one- or multi-band superconductor, the analysis starts within an ISB model. Within this model the upper critical field $H_{c2}(0)$ is given by⁵³

$$H_{c2}(0) [\text{Tesla}] = H_{c2}^{cl}(0) \left[1 + \frac{0.13\gamma_{imp} [\text{K}]}{T_c(1 + \lambda_{ph})} \right], \quad (18)$$

where

$$H_{c2}^{cl}(0) [\text{Tesla}] = 0.0237 \frac{(1 + \lambda_{ph})^{2.2} T_c^2 [\text{K}]}{v_F^2 [10^5 \frac{\text{m}}{\text{s}}]}, \quad (19)$$

and $\gamma_{imp} = v_F/l_{imp}$ is the scattering rate which determines the intrinsic resistivity (l_{imp} denotes the corresponding mean free path). The London penetration depth including the unknown impurity scattering rate γ_{imp} is given by an approximative formula

$$\begin{aligned} \lambda_L(0) &\approx \tilde{\lambda}_L(0) \sqrt{(1 + \lambda_{ph}) \left(1 + 0.7 \frac{\gamma_{imp}}{2\Delta_{exp}} \right)} \quad (20) \\ &\equiv \tilde{\lambda}_L(0) \sqrt{(1 + \lambda_{ph}) \left(1 + 0.7 \frac{\gamma_{imp}}{T_c} \frac{T_c}{2\Delta_{exp}} \right)}, \end{aligned}$$

valid for $\lambda_{ph} < 2.5$ (see App. A for the exact numerical expression), with the bare clean limit London penetration depth

$$\tilde{\lambda}_L(0) = \frac{c}{\omega_{p1}} \approx \frac{197.3 \text{ nm}}{\omega_{p1} [\text{eV}]}. \quad (21)$$

Using Eqs. (18) and (20), $\gamma_N^* = \gamma_0(1 + \lambda_{ph})$ and the experimentally determined quantities from Tab. II, we now will check the applicability of the ISB model. For this aim we consider the ratio

$$R = \frac{6.77 \times 10^{-6} \cdot \gamma_N^* \left[\frac{\text{mJ}}{\text{molK}^2} \right] \cdot \lambda_L^2(0) [\text{nm}^2] \cdot T_c^2 [\text{K}^2]}{H_{c2}(0) [\text{Tesla}] \cdot V [\text{\AA}^3]} \quad (22)$$

which includes the values of six experimentally readily accessible quantities: the Sommerfeld coefficient γ_N^* , $H_{c2}(0)$, T_c , $\lambda_L(0)$ and the volume of the unit cell. The dependence of R on the parameter γ_{imp}/T_c can be expressed as

$$R = \frac{1 + 0.35\gamma_{imp}/\Delta(0)}{(1 + \lambda_{ph})^{0.2} \{1 + 0.13\gamma_{imp}/[T_c(1 + \lambda_{ph})]\}} \quad (23)$$

In Fig. 21, the theoretical $R(\gamma_{imp}/T_c)$ curves obtained from Eq. (23) for several λ_{ph} values are compared with the value of R derived from our experimental data which is represented in Fig. 21 as horizontal line. Crossing points between the theoretical prediction and the experimental result, which confirm the applicability of the ISB, are found for $\lambda_{ph} \geq 0.8$ at low scattering rates. Even in the case of higher electron-phonon coupling constants of $\lambda_{ph} \approx 2$, a clean limit scenario with $\gamma_{imp}/T_c \approx 1$ is favored within the ISB analysis. Dirty limit (with weak or medium coupling) as proposed in Ref. 15 can be excluded from the R -check in Fig. 21.

It is noteworthy that the proposed R -check is much more convenient than the similar Q -check, proposed recently by two of the present authors,⁵³ since the dependence on λ_{ph} is considerably weaker for R and, which is more important, R does not depend on the band structure calculation. Thus comparing the results derived above with the expectations from these calculations, additional information on the nature of superconductivity in MgCNi₃, may be extracted. From Eqs. (18) and (19), the effective Fermi velocity (in 10^7 m/s)

$$\begin{aligned} v_F &= 0.154 (1 + \lambda_{ph})^{1.1} T_c [\text{K}] \times \\ &\times \sqrt{\frac{1 + 0.13\gamma_{imp} [\text{K}]/[T_c [\text{K}](1 + \lambda_{ph})]}{H_{c2}(0) [\text{Tesla}]}} \end{aligned}$$

is obtained. Using the very weak scattering rates $\gamma_{imp}/T_c \leq 1$ derived above and the experimental values $H_{c2}(0) = 11$ T and $T_c = 6.8$ K, one estimates from Eq. (24) $v_F \approx (0.60 \dots 1.08) \times 10^7$ cm/s for electron-phonon coupling constants in the range of $0.8 \leq \lambda_{ph} \leq 2.0$. Comparing this result with our band structure calculations (see Sec. II), one realizes consistency with the averaged

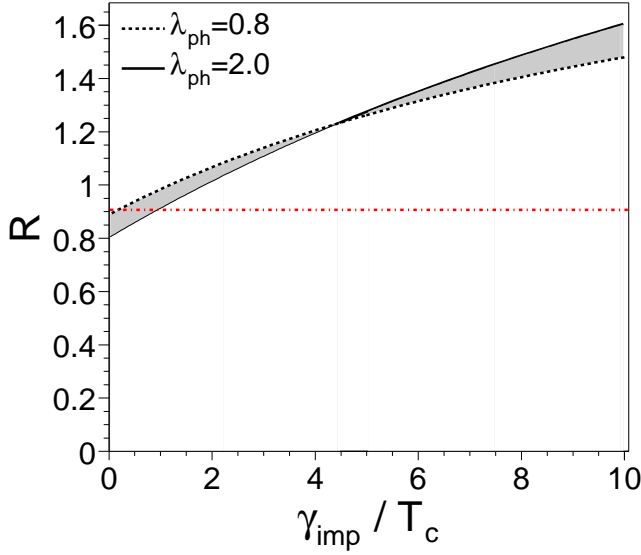


FIG. 21: Parameter R vs. γ_{imp}/T_c according to Eq. (23) in the range of electron-phonon coupling constants $0.8 \leq \lambda_{\text{ph}} \leq 2.0$. Horizontal dash-dotted line: Experimental result for $\text{MgC}_{1.6}\text{Ni}_3$ derived from Eq. (22).

$v_{\text{hc}2,\text{h}} = 1.07 \times 10^7$ m/s from the two hole Fermi surface sheets (Sec. II) for strong electron-phonon coupling of $\lambda_{\text{ph}} \approx 2.0$. Thus, the relatively high value of the upper critical field of $H_{c2}(0) = 11$ T can be attributed to strong electron-phonon coupling for the hole subsystem. The second electron band plays a minor role for $H_{c2}(0)$ due to its much faster Fermi velocities and the much lower partial density of states.

Having adopted the dominant hole picture, we also can start from the band structure results, using the Fermi velocity $v_{\text{F,h}}$ and the plasma frequency $\omega_{\text{p}1,\text{h}}$ of the hole band. Then we have to find consistent values of λ_{ph} and γ_{imp} , which describe the $H_{c2}(0)$ and $\lambda_{\text{L}}(0)$ data.

From the plasma frequency of band 1, $\hbar\omega_{\text{p}1,1} = 1.89 \dots 1.94$ eV (see Sec. II), we get $\tilde{\lambda}_{\text{L}}(0) = (101.7 \dots 104.4)$ nm, using Eq. (21). With the empirical values of $\lambda_{\text{L}}(0) = 237$ nm and $2\Delta(0) \approx 2\Delta_{\text{exp}} = 2.2$ meV $\doteq 25.5$ K for the superconducting gap (see Sec. VC), Eq. (20) depends only on γ_{imp} and $\lambda_{\text{ph,h}}$ (of the hole band). The same applies to Eq. (18), using the experimental values $H_{c2}(0) = 11$ T, $T_c = 6.8$ K and the calculated average Fermi velocity of the hole band, $v_{\text{hc}2,\text{h}} = 1.07 \times 10^7$ m/s. The correlation between γ_{imp} and $\lambda_{\text{ph,h}}$, emerging from these two equations, is shown in the left panel of Fig. 22. The intersection of both graphs gives $\lambda_{\text{ph,h}} = 1.74 \dots 1.78$ and $\gamma_{\text{imp}} = (31.0 \dots 36.0)$ K. Thus, we arrive at a higher, more realistic scattering rate compared with $\gamma_{\text{imp}} \approx T_c$ obtained from the R -check in Fig. 21. The corresponding ratio $[(H_{c2}(0)/H_{c2}^{\text{cl}}(0)) - 1]$, giving the deviation of $H_{c2}(0)$ from the clean limit value $H_{c2}^{\text{cl}}(0)$, is plotted in the right panel of Fig. 22. One gets $H_{c2}^{\text{cl}}(0) \approx (8.79 \dots 9.07)$ T.

To summarize this part, already in the simplest possi-

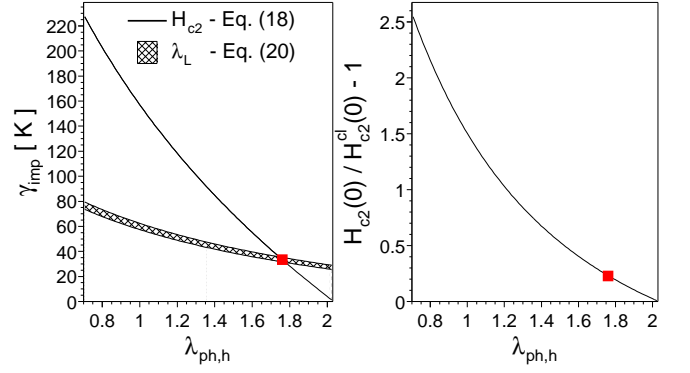


FIG. 22: Left panel: Correlation between impurity scattering rate γ_{imp} and electron-phonon coupling constant $\lambda_{\text{ph,h}}$ derived from Eq. (18) and Eq. (20) using $H_{c2}(0) = 11$ T, $T_c = 6.8$ K, $v_{\text{F}} = 1.07 \times 10^7$ m/s, $\lambda_{\text{L}}(0) = 237$ nm, $2\Delta(0) \approx 2.2$ meV. The point of intersection of both curves marked by a filled square points to an electron-phonon coupling constant of $\lambda_{\text{ph,h}} = 1.74 \dots 1.78$ in the investigated $\text{MgC}_{1.6}\text{Ni}_3$ sample. Right panel: Ratio $[(H_{c2}(0)/H_{c2}^{\text{cl}}(0)) - 1]$ plotted against $\lambda_{\text{ph,h}}$. The filled square again corresponds to $\lambda_{\text{ph,h}} = 1.74 \dots 1.78$. From $H_{c2}(0) = 11$ T one estimates $H_{c2}^{\text{cl}}(0) \approx (8.79 \dots 9.07)$ T for the upper critical field in the clean limit.

TABLE III: Characteristic phonon frequency and coupling parameters derived by analyzing the experimental data of the present $\text{MgC}_{1.6}\text{Ni}_3$ sample.

		c _p analysis		H _{c2} analysis
		normal state	sl state	
		(Sec. VB)	(Sec. VC)	(Sec. VIA)
ω_{1n}	[K]	143	88...134	
λ_{ph}		1.85	1.9...2.3	1.74...1.78 ^a
λ_{sf}		0.43		

^aLimited to band "1".

ble approach two general properties of MgCNi_3 are derived:

1. strong electron-phonon coupling and
2. intrinsic clean limit at least for the hole subsystem.

Nevertheless, it should be noted that recent preliminary measurements of the penetration depth by Lin et al.,¹⁵ resulting in $\lambda_{\text{L}}(0) = (128 \dots 180)$ nm are not compatible with the presented effective single band analysis (see also Ref. 51). Especially the R -check (Eqs. (22) and (23)) results in unphysical solutions ($\lambda_{\text{ph}} = 30$ as a lower limit), using the values presented in Ref. 15 and 51 (see as well Tab. II). The consequences, if these measurements could be verified, remain unclear.

B. Strong coupling and enhanced depairing

Several results of our analysis of the experimental data are summarized in Table III. The comparison of the esti-

mated λ_{ph} values clearly points to strong electron-phonon coupling. Nevertheless, the strong coupling scenario realized in MgCNi_3 has been questioned.^{1,15} The strong electron-phonon coupling found for MgCNi_3 requires a sizable depairing contribution to explain the low T_c value, otherwise at least a twice as large T_c would be expected. It is illustrative to compare different approaches for the calculation of T_c to analyze the electron-phonon coupling strength under consideration of the low temperature upturn of the specific heat in the normal state (see Sec. VB).

In a first approach usually the low temperature Debye approximation is used to extract the Debye temperature which we did in Sec. IV B for comparison. Our result of $\Theta_D^* = 292$ K is in agreement with previous measurements of Lin et al.,¹⁵ Mao et al.¹³ and calculations of Ignatov et al.²² (It should be noted, that our specific heat data were corrected by carbon contribution (see Fig. 3), without this correction we arrive at $\Theta_D^* = 285$ K). In this analysis the McMillan formula

$$T_c = \frac{\omega_D}{1.45} \exp \left[-1.04 \frac{1 + \lambda_{\text{ph}}}{\lambda_{\text{ph}} - \mu^* (1 + 0.62\lambda_{\text{ph}})} \right] \quad (24)$$

is usually applied. This approximation is only useful for a special phonon spectrum with $\omega_{\text{ln}}/\omega_D \approx 0.6$. In the case of MgCNi_3 we found $\approx 0.30 \dots 0.49$ (corresponding to $\omega_{\text{ln}} \approx 88 \dots 143$ K) and the Allen-Dynes formula (Eq. (6)) should be applied instead.

Fig. 23 compares both equations using $\Theta_D^* \equiv \omega_D = 292$ K (dotted line) respectively $\omega_{\text{ln}} = 143$ K (dash-dotted line). In both cases the Coulomb pseudopotential was fixed to $\mu^* = 0.13$. Apart from the deviation between Eq. (6) and Eq. (24) due to the ratio $\omega_{\text{ln}}/\omega_D \leq 0.49$, both equations seem to result in a moderate electron-phonon coupling of $\lambda_{\text{ph}} = 0.67 \dots 0.82$ if no additional pair breaking effects are considered.

However, we remind the reader, that the experimental and theoretical picture of MgCNi_3 strongly indicates strong electron-phonon coupling and a spin fluctuation contribution. The solid line compared to the dash-dotted line in Fig. 23 shows that the dependence of T_c on λ_{ph} is strongly influenced by pair-breaking contributions such as the presence of enhanced electron-paramagnon coupling $\lambda_{\text{sf}} = 0.43$. The same situation in the imaginable case of purely static pair-breaking, expressed by $\mu^* = 0.4$ is given by the dotted line. A very similar result was reported by Ignatov et al.²² who proposed a phonon-softening scenario with $T_c = 8$ K, $\omega_{\text{ln}} = 120$ K, $\lambda_{\text{ph}} = 1.51$ and an enhanced $\mu^* = 0.33$ due to spin fluctuations. In any case the superconducting transition temperature is strongly suppressed by pair-breaking contributions.

T_c of MgCNi_3 would rise up to ≈ 20 K, if one somehow could suppress the electron-paramagnon interaction. In that case the electron-phonon coupling would not be affected and the dash-dotted line in Fig. 23 would become reality.

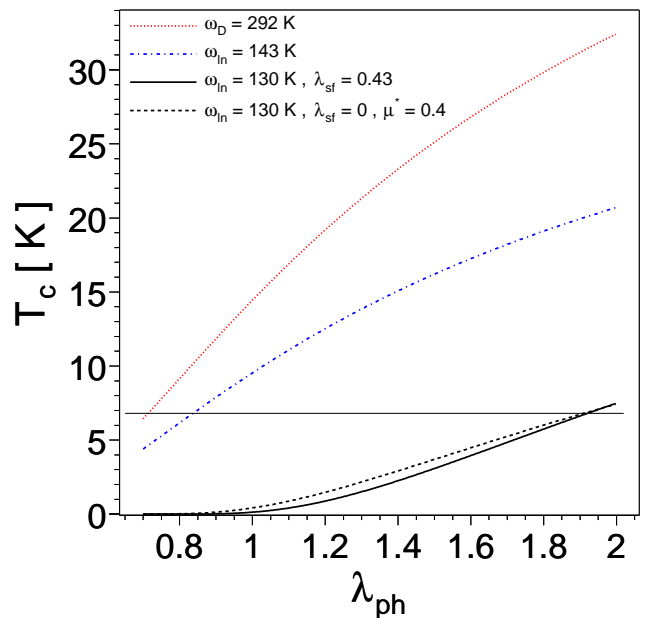


FIG. 23: Variation of T_c with λ_{ph} without electron-paramagnon interaction and “normal” Coulomb pseudopotential $\mu^* = 0.13$ according to Eq. (24) (dotted line) and Eq. (6) (dash-dotted line) and with enhanced pair-breaking contribution according to Eq. (9) by $\mu^* = 0.13$ and $\lambda_{\text{sf}} = 0.43$ (solid line), respectively $\mu^* = 0.4$ and $\lambda_{\text{sf}} = 0$ (dashed line). The characteristic phonon frequencies are chosen from Sec. IV B (dotted line), Sec. VB (dash-dotted line), respectively Sec. VC (solid and dashed line). The points of intersection of the curves with the horizontal line at $T_c = 6.8$ K show the electron-phonon coupling strengths λ_{ph} resulting in the different approaches.

Within the phonon-softening scenario,²² which was recently observed in neutron-scattering measurements,³⁷ a part of the low temperature specific heat anomaly may be of phonon origin (as stated in Sec. VB). In this picture the electron-paramagnon coupling would be reduced with the possibility of a paramagnon shift to higher temperatures. This is consistent with $\omega_{\text{ln}} \approx 100$ K (lower limit of the result from Sec. VC) and an electron-paramagnon coupling constant of $\lambda_{\text{sf}} \approx 0.25$. Using these numbers in Eq. (9) the electron-phonon coupling constant amounts $\lambda_{\text{ph}} \approx 1.6$. To find the composition of the phonon and paramagnon contribution to the upturn, low temperature neutron-scattering measurements should be performed. In this context we remind the reader, that spin fluctuations are known to show a dependence on the applied magnetic field, which indeed is seen in Fig. 12.

C. Multi-band effects beyond the standard approach

Multi- (two-) band (and similar anisotropy) effects for several physical properties in the superconducting state are in principle well known for a long time,⁵⁴ especially

for weakly coupled superconductors in the clean limit. To the best of our knowledge their interplay with disorder and strong coupling effects is less systematically studied. In particular this is caused by the increased number of input parameters and the necessity of a large amount of numerical calculations.

The multi-band character in MgCNi₃ is not only supported by the band structure calculations, but also by experimental findings, and for instance, reflected by the large gap found in tunneling measurements^{13,17} and a smaller one seen in NMR measurements.⁷

Like in MgB₂ the effect of interband scattering is expected to be weak due to the presence of well disjoint FSS. However, due to different contributions of the partial density of states compared to the case of MgB₂, the two-band character of MgCNi₃ is less pronounced. In Sec. VC the total electron-phonon coupling constant averaged over all Fermi surface sheets, $\lambda_{\text{ph,tot}}$ was estimated by Eq. (10) at $\lambda_{\text{ph,tot}} \approx 1.9$. Considering the band structure calculation presented in Sec. II, this value is to be distributed among the two contributing bands according to

$$\lambda_{\text{ph,tot}} = \lambda_{\text{h}} \frac{N_{\text{h}}(0)}{N(0)} + \lambda_{\text{el}} \frac{N_{\text{el}}(0)}{N(0)}. \quad (25)$$

With $\lambda_{\text{ph,h}} = 1.74 \dots 1.78$ (see Sec. VIA), the coupling in the second band amounts $\lambda_{\text{ph,el}} = 2.58 \dots 2.81$. Obviously this strong mass enhancement in both bands is not compatible with the low value of $T_{\text{c}} = 6.8$ K. So, as in the single band case a pair breaking contribution is needed.

Measurable quantities describing the superconducting transition in the case of MgCNi₃ (particularly Eqs. (14)) are affected in opposite ways by strong coupling effects from one side and two-band effects from the other sides. Here we will briefly show, how these different effects influence the specific heat jump $\Delta c / \gamma_{\text{N}} T_{\text{c}}$ according to Eq. (14b). Considering these effects,

$$\frac{\Delta c}{\gamma T_{\text{c}}} = 1.43 F(\mu^*) \frac{B_1 \left(\frac{\omega_{\text{ln,h}}}{T_{\text{c}}} \right) (1 + \eta v / z^2)^2}{(1 + v) (1 + \eta v / z^4)} \quad (26)$$

is derived, where

$$v = \frac{(1 + \lambda_{\text{ph,el}}) N_{\text{el}}}{(1 + \lambda_{\text{ph,h}}) N_{\text{h}}} \quad (27)$$

contains electron-phonon coupling and multi-band corrections and

$$z = \frac{\Delta_{\text{h}}}{\Delta_{\text{el}}} \quad (28)$$

denotes the gap-ratio. The function $F(\mu^*)$, given by

$$F(\mu^*) = \frac{1.15 [1 + 0.156 \tanh(5\mu^*)]}{1 + 0.156 \tanh(0.5)}$$

has been obtained by analyzing numerical data derived by Carbotte²⁰ under consideration of enhanced pair-breaking in terms of the Coulomb pseudopotential μ^*

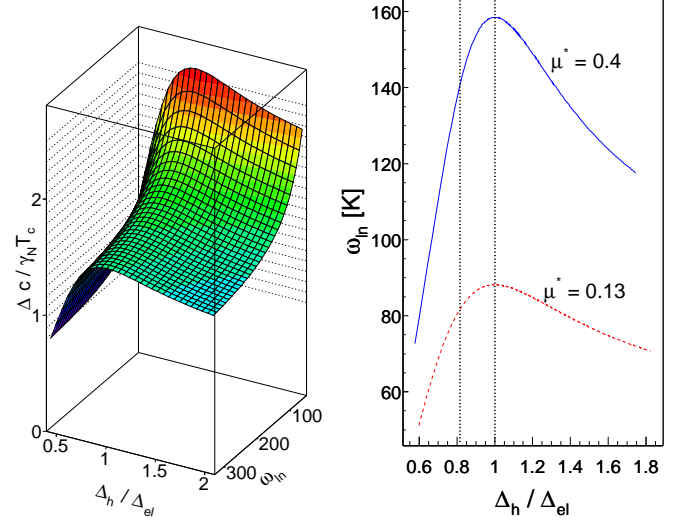


FIG. 24: Left panel: Dependence of the specific heat jump $\Delta c / \gamma_{\text{N}} T_{\text{c}}$ on the gap ratio $\Delta_{\text{h}} / \Delta_{\text{el}}$ and the characteristic phonon frequency ω_{ln} within the two-band description for $\mu^* = 0.13$ (Eq. (26)). Right panel: Possible solutions for $\Delta_{\text{h}} / \Delta_{\text{el}}$ and ω_{ln} to reach the experimental specific heat jump for the two cases $\mu^* = 0.13$ and $\mu^* = 0.4$ (enhanced pair-breaking). The two vertical lines mark the range of expected $\Delta_{\text{h}} / \Delta_{\text{el}}$ values (see Sec. VC).

(valid up to $\mu^* \approx 0.4$). The different electron-phonon coupling constants in both bands may involve different characteristic phonon frequencies ω_{ln} . This situation is formally taken into account by the parameter η , given by

$$\eta = B_1 \left(\frac{\omega_{\text{ln,el}}}{T_{\text{c}}} \right) / B_1 \left(\frac{\omega_{\text{ln,h}}}{T_{\text{c}}} \right).$$

The general result, depending on the gap ratio z and the characteristic phonon frequency ω_{ln} (for simplification $\omega_{\text{ln,el}} = \omega_{\text{ln,h}}$ is assumed) is shown in the left panel of Fig. 24 (with $\lambda_{\text{ph,h}} = 1.76$, $\lambda_{\text{ph,el}} = 2.7$ and $F(\mu^*) = 1$). The opposite effect of strong coupling from one side and two-band behavior from the other side is clearly seen. The right panel shows possible solutions for z and ω_{ln} to reach the experimental determined jump $\Delta c / \gamma_{\text{N}} T_{\text{c}} = 2.09$. Considering the results from the normal state specific heat analysis ($\omega_{\text{ln}} \approx 143$ K) and the superconducting specific heat analysis ($1 \leq z \leq 0.8$), best consistency is obtained with $\mu^* \approx 0.4$ in full agreement with the pair-breaking scenario.

Now, the influence of two-band corrections on the penetration depth $\lambda_{\text{L}}(0)$ should be checked, since the experimental value of $\lambda_{\text{L}}(0) = 237$ nm was ascribed to the hole band in Sec. VIA. We start with the inverse squared total penetration depth of a two-band superconductor. It is given as a sum of the two corresponding contributions from each band:

$$\lambda_{\text{tot}}^{-2}(0) = f_{\text{h}} \lambda_{\text{h}}^{-2}(0) + f_{\text{el}} \lambda_{\text{el}}^{-2}(0),$$

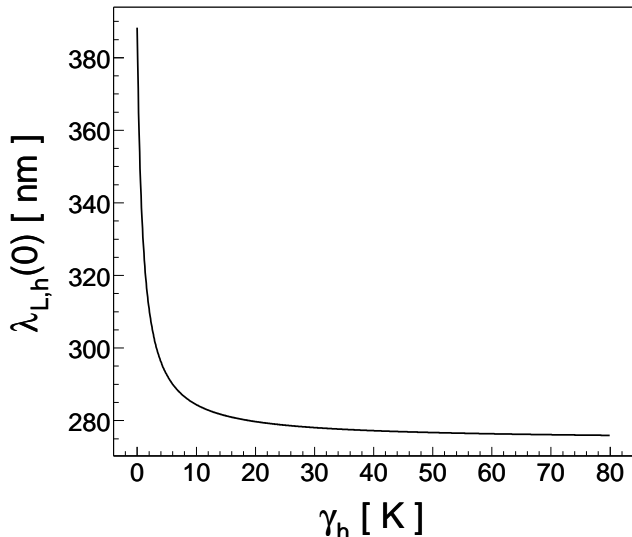


FIG. 25: Penetration depth at zero temperature derived from Eq. (29) vs. scattering rate in the hole band using $\gamma_{el}/\gamma_h \approx 4.81$ (see Eq. (1)).

with the gap ratio dependent weighting factors $f_i(z, \lambda_i, N_i)$, where $i = h, el$ and $f_i \equiv 1$ in the case of equal gaps (i.e. $z = 1$). The corresponding specific plasma frequencies, coupling constants, and gaps do enter each term (see Eqs. (20,21)). Then the total penetration depth can be rewritten as

$$\lambda_{L,h}(0) = \lambda_L(0) \times \sqrt{L \left[1 + \frac{\Delta_{el}^2 \omega_{pl,el}^2 (1 + \lambda_h) \left(1 + \frac{0.7\gamma_h}{2\Delta_h}\right)}{\Delta_h^2 \omega_{pl,h}^2 (1 + \lambda_{el}) \left(1 + \frac{0.7\gamma_{el}}{2\Delta_{el}}\right)} \right]} \quad (29)$$

with

$$L = \frac{1 + \nu/z^2}{1 + \nu/z^4}.$$

With the above determined values, we get $L \approx 0.88$ (with ν and z according to Eqs. (27,28)). Fig. 25 shows the contribution of the hole band to $\lambda_L(0)$ for the LDA calculation, using $\gamma_{el}/\gamma_h \approx 4.81$ (see Eq. (1)). It is seen, that $\lambda_{L,h}(0)$ exceeds the experimental value of $\lambda_L(0) = 237$ nm by no more than $\approx 18\%$ (in the case of $\gamma_h = 31.0 \dots 36.0$ K – see Sec. VIA), indicating only small influence of the electron band on $\lambda_L(0)$. Nevertheless its influence is not as small as in the case of $Hc_2(0)$ and thus, we estimate an error of about $\approx 10\%$ for the electron-phonon coupling constant of the hole band, determined in Sec. VIA.

VII. CONCLUSIONS

Our analysis of $MgCNi_3$ revealed a highly interesting interplay of different, on first glance unexpected adversed

physical features or tendencies all present within one material causing a rather complex general behavior. This novel superconductor has been interpreted so far as standard *s*-wave BCS superconductor or as unconventional superconductor with strong or medium electron-phonon coupling. Last but not least, considerable pair-breaking contribution due to spin fluctuations and / or Coulomb repulsion have been suggested from theory and experiment.

The present analysis is the first approach to reconcile the unusual experimental findings within a unified physical picture. It reveals strong electron-phonon coupling combined with medium electron-paramagnon coupling. Strong electron-phonon coupling was derived from specific heat data in the normal and superconducting state independently. An unusual upturn of the specific heat in the normal state observed at low temperatures can be attributed to spin fluctuations and / or a softening of low-frequency phonons. To specify the contribution of the belonging electron-boson interactions to the low temperature specific heat anomaly, low-temperature neutron measurements are necessary in order to investigate the evolution of the lattice excitations, which may even be modified by the transition from the normal to the superconducting state.

The electronic specific heat data show an exponential temperature dependence at low temperatures which is a strong indication for *s*-wave superconductivity in $MgCNi_3$. It was shown that a contribution of a second band could not be excluded but even complies with recent tunneling measurement results. The multi-band character of $MgCNi_3$ is proved by band structure calculations. However, with respect to superconductivity the two-band character of $MgCNi_3$ is much less pronounced than in the model compound MgB_2 . That is due to the predominance of a hole band with a large density of states in $MgCNi_3$, whereas in MgB_2 the densities of states of both bands are comparable. Therefore, several properties such as the specific heat or the upper critical field can be described to first approximation reasonably well within an effective single band model. Nevertheless, other properties such as the Hall conductivity and the thermopower require a multi-band description, i.e. at least one effective electron and one effective hole band (see App. B). Previous theoretical analyses based on single-band models could describe only few physical properties. As a consequence of the oversimplified approaches they blamed the local density approximation to fail seriously. This is in sharp contrast to our analysis of the upper critical field yielding an effective Fermi velocity agreeing well with the LDA hole band prediction. Our proposed effective strong coupling two-band approach explains the complex behavior observed for $MgCNi_3$ and is expected to hold for other still not examined physical properties.

The highly interesting interplay of strong electron-phonon coupling on multiple Fermi surface sheets, softening of lattice excitations, the strong energy dependence of the density of states near the Fermi energy

of one band (van Hove singularity), and paramagnons or strong Coulomb repulsion for a realistic, anisotropic multi-band electronic structure with nesting features in this compound highly motivates further experimental studies. Investigating the influence of impurities or slight stoichiometry-deviations on the electronic and bosonic properties would be as helpful as making of purer samples and single crystals to perform quantum oscillation studies like de Haas van Alphen measurements.

Deepened theoretical studies are needed to clarify remaining quantitative details and to extend the present-day strong coupling Eliashberg theory with all peculiarities of MgCNi_3 .

APPENDIX A: PENETRATION DEPTH : STRONG COUPLING AND IMPURITY SCATTERING

We present a simple semi-analytic expression for the penetration depth at $T = 0\text{K}$ for type-II superconductors valid in the London limit. Thereby strong coupling and impurity scattering effects are treated on equal footing within standard Eliashberg theory. In calculating $\lambda_L(0)$ we start from an expression proposed first by Nam⁵⁵ and later on frequently used in the literature^{56,57,58}

$$\lambda_L^{-2}(0) = \frac{\pi T \omega_{\text{pl}}^2}{c^2} \sum_{n=1}^{\infty} \frac{\Delta^2(i\omega_n)}{Z(i\omega_n) [\omega_n^2 + \Delta^2(i\omega_n)]^{3/2}}, \quad (\text{A1})$$

where $i\omega_n = i\pi(2n-1)T$, $n = 0, \pm 1, \pm 2, \dots$ are the Matsubara frequencies and $Z(i\omega_n)$ as well as $\Delta(i\omega_n)$ denote the renormalization factor and the gaps, respectively. The result of our numerical calculations of Eq. (A1) compared with the approximation given by Eq. (20) is shown in Fig. 26.

One realizes only small deviations not exceeding 8 to 10 % which is sufficient for our qualitative estimate of large mean free paths l_{imp} compared with the coherence length $\xi_{\text{GL}}(0)$.

APPENDIX B: TWO-BAND INFLUENCE ON OTHER PHYSICAL QUANTITIES

With the help of the two-band scenario even difficulties found explaining Hall data can be overcome.^{8,14} Within the two-band model (Sec. II) the Hall constant is defined as

$$R_{\text{H}} = \frac{R_{\text{H,el}}\sigma_{\text{el}}^2 + R_{\text{H,h}}\sigma_{\text{h}}^2}{(\sigma_{\text{el}} + \sigma_{\text{h}})^2},$$

using $R_{\text{H,el}} = -R_{\text{H,h}}$ with $n_{\text{h}} = n_{\text{el}}$ (due to the even number of electrons per unit cell) and the ratio of the hole and electron conductivities

$$x = \frac{\sigma_{\text{h}}}{\sigma_{\text{el}}} \approx \frac{N_{\text{h}}v_{\text{F,h}}^2\gamma_{\text{el}}}{N_{\text{el}}v_{\text{F,el}}^2\gamma_{\text{h}}},$$

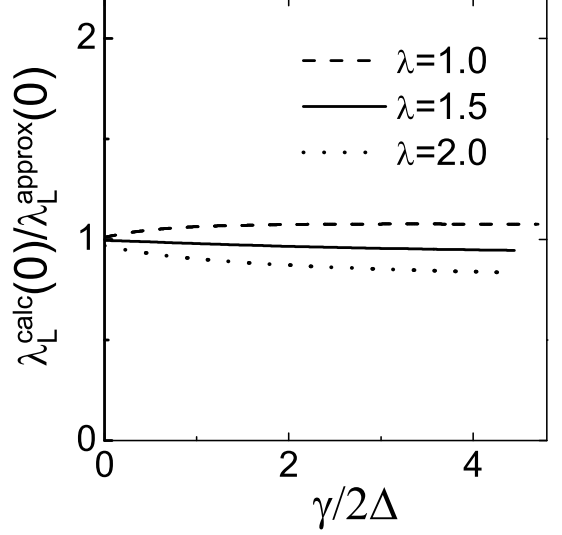


FIG. 26: Results of strong coupling calculations for the penetration depth at zero temperature (Eq. (A1)) for several electron-phonon coupling constants λ vs. impurity scattering rate γ_{imp} (in units of the gap $\Delta_{\text{exp}} = 1.1$ meV as derived from Sec. V C) in comparison with the approximate expression provided by Eq. (20).

where γ_{h} and γ_{el} are the corresponding scattering rates, we get

$$R_{\text{H}} = R_{\text{H,el}} \frac{1-x}{1+x}, \quad (\text{B1})$$

with $R_{\text{H,el}} = -1/(n_{\text{el}}ec)$. The number of charges per unit cell from LDA-FPLO calculations (see Sec. II) amounts $n = 0.285$ (comparable to $n = 0.303$ of Ref. 9). The resulting theoretical charge carrier density of $n_{\text{el}} \approx 5.2 \times 10^{21}/\text{cm}^3$ and the calculated conductivity ratio of $x = 1.403$ (see Sec. II) should now be compared with measurements in terms of the effective Hall constant given by Eq. (B1).

Since so far reported samples are widely spread in terms of their residual resistivities, grain boundary effects, affecting the Hall conductivity should be taken into account. This can be done in a first approximation by analyzing the mean free path (Eq. (4)), considering the hole subsystem

$$l_{\text{imp,h}} = 4.9 \times 10^2 \frac{v_{\text{F,h}} [10^7 \text{ cm/s}]}{(\omega_{\text{pl,h}} [\text{eV}])^2 \rho_0 (1 + \frac{1}{x}) [\mu\Omega\text{cm}]}$$

Similar considerations should be applied to the analysis of the thermopower, where also an effective electronic behavior has been observed.¹⁰

Acknowledgments

The DFG (SFB 463), the DAAD (H.R.) and the NSF (DMR-0114818) are gratefully acknowledged for financial

support. We thank A. Ignatov for providing us with Fig. 11(b) and S. Savrasov, A. Ignatov, I. Mazin, W. Pickett and T. Mishonov for discussions.

-
- * Electronic address: fuchs@ifw-dresden.de (G.Fuchs)
 † On leave from: Int Lab. of High Magn. Fields, Wroclaw; ISSP-BAS, Sofia, Bulgaria.
 ‡ On leave from Inst. for High Pressure Physics, Troitsk, 142190, Russia.
 § On leave from Inst. of Spectroscopy, Troitsk, 142190, Russia.
- ¹ T. He, Q. Huang, A. P. Ramirez, Y. Wang, K. A. Regan, N. Rogado, M. A. Hayward, M. K. Haas, J. S. Slusky, K. Inumara, et al., *Nature* **411**, 54 (2001).
 - ² H. Rosner, R. Weht, M. D. Johannes, W. E. Pickett, and E. Tosatti, *Phys. Rev. Lett.* **88**, 027001 (2002).
 - ³ S. B. Dugdale and T. Jarlborg, *Phys. Rev. B* **64**, 100508(R) (2001).
 - ⁴ D. J. Singh and I. I. Mazin, *Phys. Rev. B* **64**, 140507(R) (2001).
 - ⁵ A. Szajek, *J. Phys.: Condens. Matter* **13** (26), L595 (2001).
 - ⁶ J. H. Shim, S. K. Kwon, and B. I. Min, *Phys. Rev. B* **64**, 180510(R) (2001).
 - ⁷ P. M. Singer, T. Imai, T. He, M. A. Hayward, and R. J. Cava, *Phys. Rev. Lett.* **87**, 257601 (2001).
 - ⁸ S. Y. Li, R. Fan, X. H. Chen, C. H. Wang, W. Q. Mo, K. Q. Ruan, Y. M. Xiong, X. G. Luo, H. T. Zhang, L. Li, et al., *Phys. Rev. B* **64**, 132505 (2001).
 - ⁹ T. G. Kumary, J. Janaki, A. Mani, S. M. Jaya, V. S. Sastry, Y. Hariharan, T. S. Radhakrishnan, and M. C. Valsakumar, *Phys. Rev. B* **66**, 064510 (2002).
 - ¹⁰ S. Y. Li, W. Q. Mo, M. Yu, W. H. Zheng, C. H. Wang, Y. M. Xiong, R. Fan, H. S. Yang, B. M. Wu, L. Cao, et al., *Phys. Rev. B* **65**, 064534 (2002).
 - ¹¹ M. A. Hayward, M. K. Haas, A. P. Ramirez, T. He, K. A. Regan, N. Rogado, K. Inumara, and R. J. Cava, *Solid State Commun.* **119**, 491 (2001).
 - ¹² S. Y. Li, R. Fan, X. H. Chen, C. H. Wang, W. Q. Mo, K. Q. Ruan, Y. M. Xiong, X. G. Luo, H. T. Zhang, L. Li, et al., *cond-mat/0104554v1*.
 - ¹³ Z. Q. Mao, M. M. Rosario, K. D. Nelson, K. Wu, I. G. Deac, P. Schiffer, Y. Liu, T. He, K. A. Regan, and R. J. Cava, *Phys. Rev. B* **67**, 094502 (2003).
 - ¹⁴ D. P. Young, M. Moldovan, D. D. Craig, P. W. Adams, and J. Y. Chan, *Phys. Rev. B* **68**, 020501 (2003).
 - ¹⁵ J.-Y. Lin, P. L. Ho, H. L. Huang, P. H. Lin, Y.-L. Zhang, R.-C. Yu, C.-Q. Jin, and H. D. Yang, *Phys. Rev. B* **67**, 052501 (2003).
 - ¹⁶ L. Shan, K. Xia, Z. Y. Liu, H. H. Wen, Z. A. Ren, G. C. Che, and Z. X. Zhao, *Phys. Rev. B* **68**, 024523 (2003).
 - ¹⁷ L. Shan, H. J. Tao, H. Gao, Z. Z. Li, Z. A. Ren, G. C. Che, and H. H. Wen, *Phys. Rev. B* **68**, 144510 (2003).
 - ¹⁸ R. Prozorov, A. Snezhko, T. He, and R. J. Cava, *Phys. Rev. B* **68**, 180502(R) (2003).
 - ¹⁹ D. P. Young, M. Moldovan, and P. W. Adams, *cond-mat/0312651v1*.
 - ²⁰ J. P. Carbotte, *Rev. Mod. Phys.* **62**, 1027 (1990).
 - ²¹ I. R. Shein, A. L. Ivanovskii, E. Z. Kurmaev, A. Moewes, S. Chiuzbian, L. D. Finkelstein, M. Neumann, Z. A. Ren, and G. C. Che, *Phys. Rev. B* **66**, 024520 (2002).
 - ²² A. Yu. Ignatov, S. Y. Savrasov, and T. A. Tyson, *Phys. Rev. B* **68**, 220504(R) (2003).
 - ²³ K. Koepf and H. Eschrig, *Phys. Rev. B* **59**, 1743 (1999).
 - ²⁴ Rietveld refinement program FULLPROF2000.
 - ²⁵ Z. A. Ren, G. C. Che, S. L. Jia, H. Chen, Y. M. Ni, G. D. Liu, and Z. X. Zhao, *Physica C* **371**, 1 (2002).
 - ²⁶ P. H. Keesom and N. Pearlman, *Phys. Rev.* **99**, 1119 (1955).
 - ²⁷ G. Fuchs, K.-H. Müller, A. Handstein, K. Nenkov, V. N. Narozhnyi, D. Eckert, M. Wolf, and L. Schultz, *Sol. State Comm.* **118**, 497 (2001).
 - ²⁸ N. R. Werthammer, E. Helfand, and P. C. Hohenberg, *Phys. Rev.* **147**, 295 (1966).
 - ²⁹ A. F. Ioffe and A. R. Regel, *Prog. Semicond.* **4**, 237 (1960).
 - ³⁰ N. F. Mott, *Philos. Mag.* **26**, 1015 (1972).
 - ³¹ A. Karkin, B. Goshchitskii, E. Kurmaev, Z. A. Ren, and G. C. Che, *cond-mat/0209575*.
 - ³² C. Kittel, *Introduction to solid state physics* (Wiley, 1996), 7th ed.
 - ³³ G. P. Srivastava, *The Physics of Phonons* (Adam Hilger, 1990).
 - ³⁴ A. Junod, T. Jarlborg, and J. Muller, *Phys. Rev. B* **27**, 1568 (1983).
 - ³⁵ S. Manalo, H. Michor, M. El-Hagary, and G. Hilscher, *Phys. Rev. B* **63**, 104508 (2001).
 - ³⁶ P. B. Allen and R. C. Dynes, *Phys. Rev. B* **12**, 905 (1975).
 - ³⁷ R. Heid, B. Renker, H. Schober, P. Adelman, D. Ernst, and K.-P. Bohnen, *cond-mat/0310592v1*.
 - ³⁸ D. Rainer, *Prog. Low Temp. Phys.* **10**, 371 (1986).
 - ³⁹ G. Gladstone, M. A. Jensen, and J. R. Schrieffer, *Superconductivity* (Dekker, 1969).
 - ⁴⁰ H. Michor, R. Krendelsberger, G. Hilscher, E. Bauer, C. Dusek, R. Hauser, L. Naber, D. Werner, P. Rogl, and H. W. Zanbergen, *Phys. Rev. B* **54**, 9408 (1996).
 - ⁴¹ B. Mühlischlegel, *Z. f. Physik* **155**, 313 (1959).
 - ⁴² J. E. Sonier, M. F. Hundley, J. D. Thompson, and J. W. Brill, *Phys. Rev. Lett.* **82**, 4914 (1998).
 - ⁴³ D. A. Wright, J. P. Emerson, B. F. Woodfield, J. E. Gordon, R. A. Fisher, and N. E. Phillips, *Phys. Rev. Lett.* **82**, 1550 (1999).
 - ⁴⁴ A. P. Ramirez, N. Stücheli, and E. Bucher, *Phys. Rev. Lett.* **74**, 1218 (1995).
 - ⁴⁵ M. Hedo, *J. Phys. Soc. Japan* **67**, 272 (1998).
 - ⁴⁶ M. Nohara, M. I. F. Sakai, and H. Takagi, *J. Phys. Soc. Japan* **68**, 1078 (1999).
 - ⁴⁷ M. Nohara, M. Isshiki, H. Takagi, and R. J. Cava, *J. Phys. Soc. Japan* **66**, 1888 (1997).
 - ⁴⁸ D. Lipp, M. Schneider, A. Gladun, S.-L. Drechsler, J. Freudenberger, G. Fuchs, K. Nenkov, K.-H. Müller, T. Cichorek, and P. Gegenwart, *Europhys. Lett.* **58**, 435 (1998).
 - ⁴⁹ K. Izawa, A. Shibata, Y. Matsuda, Y. Kato, H. Takeya,

- K. Hirata, C. J. van der Beek, and M. Konczykowski, Phys. Rev. Lett. **86**, 1327 (2001).
- ⁵⁰ E. Boaknin, R. W. Hill, C. Proust, C. Lupien, L. Taillefer, and P. C. Canfield, Phys. Rev. Lett. **87**, 237001 (2001).
- ⁵¹ J.-Y. Lin and H. D. Yang, cond-mat/0308198.
- ⁵² C. Q. Jin, Y. L. Zhang, Z. X. Liu, F. Y. Li, W. Yu, and R. C. Yu, Physica C **388-389**, 561 (2003).
- ⁵³ S. V. Shulga and S.-L. Drechsler, J. Low Temp. Phys. **129** (1-2), 93 (2002).
- ⁵⁴ V. A. Moskalenko and M. E. Palistrant, *Statistical Physics and Quantum Field Theory* (Nauka [in russian], 1973).
- ⁵⁵ S. B. Nam, Phys. Rev. **156**, 470 (1967).
- ⁵⁶ F. Marsiglio, J. P. Carbotte, and J. Blezius, Phys. Rev. B **41**, 6457 (1990).
- ⁵⁷ S. D. Adrian, M. E. Reeves, S. A. Wolf, and V. Z. Kresin, Phys. Rev. B **51**, 6800 (1995).
- ⁵⁸ A. A. Golubov, A. Brinkman, O. V. Dolgov, J. Kortus, and O. Jepsen, Phys. Rev. B **66**, 054524 (2002).